The new Kr-86 excess ice core proxy for synoptic activity: West Antarctic storminess possibly linked to ITCZ movement through the last deglaciation

Christo Buizert[1], Sarah Shackleton[2], Jeffrey P. Severinghaus[2], William H. G. Roberts[3], Alan Seltzer[2,4], Bernhard Bereiter[5], Kenji Kawamura[6], Daniel Baggenstos[5], Anaïs J. Orsi[7,8], Ikumi Oyabu[6], Benjamin Birner[2], Jacob D. Morgan[2], Edward J. Brook[1], David M. Etheridge[9,10], David Thornton[9,10], Nancy Bertler[11,12], Rebecca L. Pyne[11], Robert Mulvaney[13], Ellen Mosley-Thompson[14], Peter D. Neff[15,16], and Vasilii V. Petrenko[16]

[1]College of Earth, Ocean and Atmospheric Sciences, Oregon State University, Corvallis, OR 97331, USA
[2]Scripps Institution of Oceanography, University of California San Diego, La Jolla, CA 92093, USA
[3]Geography and Environmental Sciences, Northumbria University, Newcastle, UK and BRIDGE, School of Geographical Sciences, University of Bristol, Bristol, UK
[4]Marine Chemistry and Geochemistry Department, Woods Hole Oceanographic Institution, Woods Hole, MA 02543, USA
[5]Climate and Environmental Physics, Physics Institute, and Oeschger Center for Climate Research, University of Bern, 3012, Bern, Switzerland
[6]National Institute for Polar Research, 10-3 Midori-cho, Tachikawa, Tokyo 190-8518, Japan
[7]Laboratoire des Sciences du Climat et de l'Environnement, LSCE/IPSL, CEA-CNRS-UVSQ, Université Paris-Saclay,l'Orme des merisiers, Gif-sur-Yvette, France
[8]Earth, Ocean and Atmospheric Sciences Department, The University of British Columbia, Vancouver, BC V6T 1Z4, Canada
[9]CSIRO Environment, PMB 1, Aspendale, Victoria 3195, Australia
[10]Australian Antarctic Program Partnership, Institute for Marine & Antarctic Studies, University of Tasmania, Hobart, Tasmania 7004, Australia
[11]Antarctic Research Centre, Victoria University of Wellington, Wellington, 6012, New Zealand
[12]GNS Science, Lower Hut 5010, New Zealand
[13]British Antarctic Survey, National Environment Research Council, Cambridge CB3 0ET, UK
[14]Byrd Polar and Climate Research Center, The Ohio State University, Columbus, OH 43210, USA
[15]Department of Soil, Water, and Climate, University of Minnesota, Saint Paul, MN 55108, USA
[16]Department of Earth and Environmental Sciences, University of Rochester, Rochester, NY 14627, USA

Correspondence to: Christo Buizert (christo.buizert@oregonstate.edu)

Abstract

Here we present a newly developed ice core gas-phase proxy that directly samples a component of the large-scale atmospheric circulation: synoptic-scale pressure variability. Surface pressure changes weakly disrupt gravitational isotopic settling in the firn layer, which is recorded in krypton-86 excess ($^{86}Kr_{xs}$). The $^{86}Kr_{xs}$ ~~reflects~~may therefore reflect the time-averaged synoptic pressure variability over several years (site "storminess"), ~~and does not~~but it likely cannot record individual synoptic events as ice core gas samples typically average over several years. We validate $^{86}Kr_{xs}$ using late Holocene ice samples from eleven Antarctic and one Greenland ice core that collectively represent a wide range of surface pressure variability in the modern climate. We find a strong spatial correlation ($r = -0.94$, $p < 0.01$) between site-average $^{86}Kr_{xs}$ and time-averaged synoptic variability from reanalysis data. The main uncertainties in the analysis are the corrections for gas loss and thermal fractionation, and the relatively large scatter in the data. Limited scientific understanding of the firn physics and potential biases of $^{86}Kr_{xs}$ require caution in interpreting this proxy at present. We show that Antarctic $^{86}Kr_{xs}$ ~~is~~appears to be linked to the position of the southern hemisphere eddy-driven subpolar jet (SPJ), with a southern position enhancing pressure variability.

We present a $^{86}Kr_{xs}$ record covering the last 24 ka from the WAIS Divide ice core. Based on the empirical spatial correlation of synoptic activity and $^{86}Kr_{xs}$ at various Antarctic sites, we interpret this record to show that West Antarctic synoptic activity is slightly below modern levels during the last glacial maximum (LGM); increases during the Heinrich Stadial 1 and Younger Dryas North Atlantic cold periods; weakens abruptly at the Holocene onset; remains low during the early and mid-Holocene, and gradually increases to its modern value. The WAIS Divide $^{86}Kr_{xs}$ record resembles records of monsoon intensity thought to reflect changes in the meridional position of the intertropical convergence zone (ITCZ) on orbital and millennial timescales, such that West Antarctic storminess is weaker when the ITCZ is displaced northward, and stronger when it is displaced southward. We interpret variations in synoptic activity as reflecting movement of the South Pacific SPJ in parallel to the ITCZ migrations, which is the expected zonal-mean response of the eddy-driven jet in models and proxy data. Past changes to Pacific climate and the El Niño Southern Oscillation (ENSO) may amplify the signal of the SPJ migration. Our interpretation is broadly consistent with opal flux records from the Pacific Antarctic zone thought to reflect wind-driven upwelling.

We emphasize that $^{86}Kr_{xs}$ is a new proxy, and more work is called for to confirm, replicate and better understand these results; until such time, our conclusions regarding past atmospheric dynamics remain speculative. Current scientific understanding of firn air transport and trapping is insufficient to explain all the observed variations in $^{86}Kr_{xs}$. A list of suggested future studies is provided.

1 Introduction

1.1 Motivation and objectives

Proxy records from around the globe show strong evidence for past changes in Earth's atmospheric circulation and hydrological cycle that often far exceed those seen in the relatively short instrumental period.

For example, low-latitude records of riverine discharge captured in ocean sediments (Peterson et al., 2000), and isotopic composition of meteoric water captured in dripstone calcite (Cheng et al., 2016), suggest large variations in tropical hydrology and monsoon strength, commonly interpreted as meridional migrations of the intertropical convergence zone or ITCZ (Chiang and Friedman, 2012; Schneider et al., 2014). Such ITCZ movement is seen both in response to insolation changes linked to planetary orbit (Cruz et al., 2005) as well as in response to the abrupt millennial-scale Dansgaard-Oeschger (D-O) and Heinrich cycles of the North-Atlantic (Kanner et al., 2012; Wang et al., 2001); the organizing principle is that the ITCZ follows the thermal equator and therefore migrates towards the warmer (or warming) hemisphere (Broccoli et al., 2006; Chiang and Bitz, 2005).

As a second example, the intensity of the El Niño – Southern Oscillation (ENSO), the dominant mode of global interannual climate variability, has changed through time. A variety of proxy data suggest ENSO activity in the 20th century was much stronger than in preceding centuries (Emile-Geay et al., 2015; Fowler et al., 2012; Gergis and Fowler, 2009; Thompson et al., 2013). The vast majority of data and model studies suggest weakened ENSO strength in the mid- and early-Holocene, likely in response to stronger orbitally-driven NH summer insolation at that time (Braconnot et al., 2012; Cane, 2005; Clement et al., 2000; Driscoll et al., 2014; Koutavas et al., 2006; Liu et al., 2000; Liu et al., 2014; Moy et al., 2002; Rein et al., 2005; Tudhope et al., 2001; Zheng et al., 2008); yet other studies suggest there may not be such a clear trend, and simply more variability (Cobb et al., 2013). Intensification of ENSO (or perhaps a more El-Niño-like mean state) may have occurred during the North-Atlantic cold phases of the abrupt D-O and Heinrich cycles (Braconnot et al., 2012; Merkel et al., 2010; Stott et al., 2002; Timmermann et al., 2007). Overall, understanding past and future ENSO variability remains extremely challenging (Cai et al., 2015).

As a last example, the strength and meridional position of the southern hemisphere westerlies (SHW) is thought to have changed in the past, which, via Southern Ocean wind-driven upwelling, has potential implications for the global overturning circulation (Marshall and Speer, 2012) and for carbon storage in the abyssal ocean (Anderson et al., 2009; Russell et al., 2006; Toggweiler et al., 2006). The SHW are thought to be shifted equatorward (Kohfeld et al., 2013) during the last glacial maximum (LGM), a shift on which climate models disagree (Rojas et al., 2009; Sime et al., 2013). During the abrupt D-O and Heinrich cycles, the SHW move in parallel with the aforementioned migrations of the ITCZ in both data (Buizert et al., 2018; Marino et al., 2013; Markle et al., 2017) and models (Lee et al., 2011; Pedro et al., 2018; Rind et al., 2001).

As these examples clearly illustrate, evidence of past changes to the large-scale atmospheric circulation is widespread. However, proxy evidence of such past changes is typically indirect – for example via isotopes in precipitation, sea surface temperature, ocean frontal positions, windblown dust, or ocean upwelling – complicating their interpretation. Here we present a newly developed noble gas-based ice core proxy, Kr-

102 86 excess (^{86}Kr$_{xs}$), that directly samples a component of the large-scale atmospheric circulation: synoptic-
103 scale pressure variability. Owing to the firn air residence time of several years (Buizert et al., 2013) and the
104 gradual bubble trapping process, each ice core sample contains a distribution of gas ages, rather than a
105 single age. Therefore, ^{86}Kr$_{xs}$ does not record the passing of individual weather systems, but rather the time-
106 average intensity of synoptic-scale barometric variability.

107 Here we provide the first complete description of this new proxy. We validate and calibrate ^{86}Kr$_{xs}$ using
108 late-Holocene ice core samples from locations around Antarctica and Greenland that represent a wide range
109 of pressure variability in the modern climate. We discuss the difficulties in using this proxy (analytical
110 precision, surface melt, corrections for sample gas loss and thermal fractionation). Next, we use reanalysis
111 data to better understand the drivers of surface pressure variability in Antarctica. Last, we present an ^{86}Kr$_{xs}$
112 records from the Antarctic WAIS Divide ice core through the last deglaciation.

113 **1.2 Gravitational disequilibrium and Kr-86 excess**

114 The upper 50-100 m of the ice sheet accumulation zone consists of firn, the unconsolidated intermediate
115 stage between snow and ice. An interconnected pore network exists within the firn, in which gas transport
116 is dominated by molecular diffusion (Schwander et al., 1993). Diffusion in this stagnant air column results
117 in gravitational enrichment in heavy gas isotopic ratios such as $\delta^{15/14}$N-N$_2$, $\delta^{40/36}$Ar and $\delta^{86/82}$Kr (Schwander,
118 1989; Sowers et al., 1992). In gravitational equilibrium, all these gases attain the same degree of isotopic
119 enrichment per unit mass difference:

120 $$\delta_{\text{grav}}(z) = \left[\exp\left(\frac{\Delta m g z}{RT}\right) - 1\right] \times 1000‰ \qquad (1)$$

121 with Δm the isotopic mass difference (1×10^{-3} kg mol^{-1}), g the gravitational acceleration, z the depth, R the
122 gas constant and T the ~~Kelvin~~ temperature in Kelvin.

123 Besides molecular diffusion, firn air is mixed and transported via three other processes: downward
124 advection with the sinking ice matrix, convective mixing (used in the firn air literature as an umbrella term
125 to denote vigorous air exchange with the atmosphere via e.g. wind pumping and seasonal convection), and
126 dispersive mixing. These last three transport processes are all driven by large-scale air movement that does
127 not distinguish between isotopologues, and we refer to them collectively as macroscopic air movement. Of
128 particular interest for our proxy is dispersive mixing, which is driven by surface pressure variations. When
129 a low-pressure (high-pressure) system moves into the site, firn air at all depth levels is forced upwards
130 (downwards) to reach hydrostatic equilibrium with the atmosphere – a process called barometric pumping.
131 One can think of the firn layer "breathing" in and out in response to a rising and falling barometer,
132 respectively. Because firn has a finite dispersivity (Schwander et al., 1988), this air movement mixes the
133 interstitial firn air ~~(Buizert and Severinghaus, 2016). The~~ . Note that also an upward air movement exists in
134 the firn column relative to the overall downward advection of the ice, which is caused by the slow reduction
135 of porosity with depth (Rommelaere et al., 1997). This upward air flow due to gradual pore closure (around
136 10^{-9} to 10^{-8} m s^{-1}) is orders of magnitude smaller than the flows driven via barometric pumping~~, and~~ (around
137 10^{-6} m s^{-1}), and therefore neglected here~~.~~ (Buizert and Severinghaus, 2016).

138 Any type of macroscopic air movement disturbs the gravitational settling, reducing isotopic enrichment
139 below δ_{grav}. Let δ^{86}Kr, δ^{40}Ar, and δ^{15}N refer to deviations of ^{86}Kr/^{82}Kr, ^{40}Ar/^{36}Ar, and ^{29}N$_2$/^{28}N$_2$, respectively,

140 from their ratios in the well-mixed atmosphere. Gases that diffuse faster (such as N_2) will always be closer
141 to gravitational equilibrium than gases that diffuse slower (such as Kr), and in the absence of thermal
142 fractionation $\delta^{86}Kr/4 < \delta^{40}Ar/4 < \delta^{15}N < \delta_{grav}$. The isotopic differences $\delta^{86}Kr/4 - \delta^{40}Ar/4$ and $\delta^{86}Kr/4 - \delta^{15}N$
143 thus reflect the degree of gravitational disequilibrium. The magnitudes of the isotopic disequilibria scale in
144 a predictable way following the molecular diffusion coefficients (Birner et al., 2018); because the diffusion
145 coefficients of N_2 and Ar are very similar, their disequilibria are comparable in magnitude. We define Kr-
146 86 excess using the Kr and Ar isotopic difference:

$$^{86}Kr_{xs40} = \frac{\delta^{86}Kr_{corr} - \delta^{40}Ar_{corr}}{\delta^{40}Ar_{corr}} \times 1000 \text{ per meg } \text{‰}^{-1} \qquad (2)$$

148 where the "corr" subscript denotes a correction for gas loss (Appendix A1) and thermal fractionation
149 (Appendix A2). The rationale for including a normalization in the denominator is discussed below. An
150 alternative Kr-86 excess definition is possible using $\delta^{15}N$ instead of $\delta^{40}Ar$:

$$^{86}Kr_{xs15} = \frac{\delta^{86}Kr_{corr}/4 - \delta^{15}N_{corr}}{\delta^{15}N_{corr}} \times 1000 \text{ per meg } \text{‰}^{-1} \qquad (3)$$

152 Note that both definitions rely on having measurements of three isotope ratios ($\delta^{86}Kr$, $\delta^{40}Ar$ and $\delta^{15}N$), as
153 the thermal correction requires $\delta^{40}Ar$ and $\delta^{15}N$ be known. The $^{86}Kr_{xs40}$ definition is preferred, because per
154 unit mass difference $\delta^{40}Ar$ is less sensitive to thermal fractionation than $\delta^{15}N$ is (Grachev and Severinghaus,
155 2003a; 2003b); this makes it more suitable for interpreting time series. Unless explicitly stated otherwise,
156 we use $^{86}Kr_{xs40}$ as our definition of Kr-86 excess. The $^{86}Kr_{xs15}$ does provide a way to check the validity of
157 $^{86}Kr_{xs40}$ timeseries, and indeed we find good correspondence between both definitions for the WDC
158 deglacial timeseries. Because the disequilibrium signal is small, we express $^{86}Kr_{xs}$ in units of per meg (parts
159 per million) of gravitational disequilibrium per ‰ of gravitational enrichment. This unit (per meg ‰$^{-1}$) is
160 mathematically identical to ‰, but we use it to emphasize the normalization in the denominator.

161 In the (theoretical) case of full gravitational equilibrium (and no gas loss or thermal fractionation), $\delta^{86}Kr/4$
162 $= \delta^{40}Ar/4 = \delta^{15}N = \delta_{grav}$, and therefore $^{86}Kr_{xs} = 0$. Any type of macroscopic mixing will cause $\delta^{86}Kr/4 <$
163 $\delta^{40}Ar/4 < \delta^{15}N < \delta_{grav}$, and thus $^{86}Kr_{xs} < 0$. In this sense $^{86}Kr_{xs}$ is a quantitative measure for the degree of
164 gravitational disequilibrium in the firn layer (Birner et al., 2018; Buizert and Severinghaus, 2016).

165 Kawamura et al. (2013) first describe this gravitational disequilibrium (or kinetic) fractionation effect at
166 the Megadunes site (Severinghaus et al., 2010), where deep firn cracking leads to a 23 m-thick convective
167 zone. They suggest that the isotopic disequilibrium can be used to estimate past convective zone thickness.
168 We show here that sites with small convective zones can nevertheless have very negative $^{86}Kr_{xs}$, and instead
169 we suggest that the ice core $^{86}Kr_{xs}$ is dominated by dispersive mixing driven by barometric pumping from
170 time-averaged synoptic-scale pressure variability.

171 The principle behind $^{86}Kr_{xs}$ is illustrated with idealized firn model experiments in Fig. 1. In the absence of
172 dispersive mixing (Fig. 1A, left panel), all isotope ratios approach δ_{grav} and $\delta^{86}Kr - \delta^{40}Ar$ is close to zero –
173 but not exactly zero owing to downward air advection. Next, we replace a fraction f of the molecular
174 diffusion with dispersive mixing. With dispersive mixing at $f = 0.1$ and $f = 0.2$ of total mixing (middle and

175   right panels, respectively), isotopic enrichment is progressively reduced below δ_{grav} (dashed line), making

176     $\delta^{86}Kr$ - $\delta^{40}Ar$ (and consequently $^{86}Kr_{xs}$) increasingly negative.

177   The ratio of macroscopic over diffusive transport is expressed via the dimensionless Péclet number, given

178   here for advection and dispersion:

179 $$\text{Pe}_X = \frac{w_{air}L + D_{disp}}{D_X} \tag{4}$$

180   where $\textbf{Pe}_X$ is the Péclet number for gas X, w_{air} the (downward) advective air velocity, L a characteristic

181   length scale, D_X the diffusion coefficient for gas X, and D_{disp} is the dispersion coefficient (Buizert and

182   Severinghaus, 2016). In agreement with earlier studies (Birner et al., 2018; Kawamura et al., 2013), we find

183   that $\delta^{86}Kr$ - $\delta^{40}Ar$ is maximized when molecular and dispersive mixing are equal in magnitude ($f = 0.5$, Fig.

184   1B), corresponding to $\textbf{Pe}_X \approx \textbf{1}$. Note that $^{86}Kr_{xs}$ responds more linearly to f than $\delta^{86}Kr$ - $\delta^{40}Ar$ does, due to

185     $\delta^{40}Ar$ in the denominator of Eq. (2).

186   In a last idealized experiment, we keep the fraction of dispersion fixed at $f = 0.1$ while we reduce the

187   thickness of the firn column by increasing the site temperature (Fig. 1C). We find that $\delta^{86}Kr$ - $\delta^{40}Ar$ scales

188   linearly with firn thickness, here represented by $\delta^{40}Ar$ on the x-axis. However, $^{86}Kr_{xs}$ remains essentially

189   constant due to the normalization by $\delta^{40}Ar$ in the denominator of Eq. (2). The normalization step is thus

190   necessary to enable meaningful comparison between different sites and time periods that all have different

191   firn thicknesses. For this reason, the definition of $^{86}Kr_{xs}$ used here has been updated from the original

192   definition by (Buizert and Severinghaus, 2016).

193   Note that these highly idealized experiments assume dispersive mixing to be a fixed fraction of total

194   transport throughout the firn column, equivalent to a constant Péclet number in the diffusive zone (a

195   convective zone is absent in these simulations). In reality, the Péclet number varies greatly on all spatial

196   scales. On the macroscopic scale (> 1 m), Pe reflects the various transport regimes (Sowers et al., 1992),

197   being highest in the convective and lock-in zones. On the microscopic scale (< 1 cm), hydraulic

198   conductance scales as $\propto r^4$ (with r the pore radius) whereas the diffusive conductance scales as $\propto r^2$. This

199   means that the Darcy flow associated with barometric pumping will concentrate in the widest pores and

200   pathways, leading to a range of effective Péclet numbers within a single sample of firn. At intermediate

201   spatial scales of a few cm, firn density layering introduces strong heterogeneity in transport properties. It is

202   unclear at present whether the competition between diffusive and non-diffusive transport, which occurs at

203   the microscopic pore level, can be accurately represented in macroscopic firn air models via a linear

204   parameterization as is the current practice.

205

2 Methods

2.1 Ice core sites

In this study we use ice samples from eleven ice cores drilled in Antarctica, and one in Greenland. The Antarctic sites are: West Antarctic Ice Sheet (WAIS) Divide core (WDC06A, or WDC), Siple Dome (SDM), James Ross Island (JRI), Bruce Plateau (BRP), Law Dome DE08, Law Dome DE08-OH, Law Dome DSSW20K, Roosevelt Island Climate Evolution (RICE), Dome Fuji (DF), EPICA (European Project for Ice Coring in Antarctica) Dome C (EDC), and South Pole Ice Core (SPC14, or SP). Ice core locations in Antarctica are shown in Fig. 2A. In Greenland, we use samples from the Greenland Ice Sheet Project 2 (GISP2).

We shall refer to late Holocene data from these sites as the calibration dataset, analogous to a core top data set in the sediment coring literature. Site characteristics, coordinates, and number of samples included in the calibration data set are given in Table 1. The DE08-OH site is a recent revisit of the Law Dome DE08 site. The DE08-OH core was measured at sub-annual resolution to understand cm-scale $^{86}Kr_{xs}$ variations due to for example layering in firn density and bubble trapping (Appendix B). In addition to the calibration data set, we present a record of Kr-86 excess going back to the LGM from WDC.

2.2 Ice sample analysis

We broadly follow analytical procedures described elsewhere (Bereiter et al., 2018a; Bereiter et al., 2018b; Headly and Severinghaus, 2007; Severinghaus et al., 2003). In short, an 800 g ice sample, its edges trimmed with a band saw to expose fresh surfaces, is placed in a chilled vacuum flask that is then evacuated for 20 minutes using a turbomolecular pump. Air is extracted from the ice by melting the sample while stirring vigorously with a magnetic stir bar, led through a water trap, and cryogenically trapped in a dip tube immersed in liquid He. Next, the sample is split into two unequal fractions. The smaller fraction (about 2% of total air) is analyzed for $\delta^{15}N-N_2$, $\delta^{18}O-O_2$, $\delta O_2/N_2$ and $\delta Ar/N_2$ on a 3kV Thermo Finnigan Delta V plus dual inlet IRMS (isotope ratio mass spectrometer). In the larger fraction, noble gases are isolated via hot gettering to remove reactive gases. The purified noble gases are then analyzed for $\delta^{40/36}Ar$, $\delta^{40/38}Ar$, $\delta^{86/82}Kr$, $\delta^{86/84}Kr$, $\delta^{86/83}Kr$, $\delta Kr/Ar$ and $\delta Xe/Ar$ on a 10kV Thermo Finnigan MAT253 dual inlet IRMS. We reject one sample from RICE due to incomplete sample transfer, and one sample from WDC due to problems with the water trap. Calibration is done for each measurement campaign by running samples of La Jolla pier air.

All calibration (core top) data were measured using "Method 2" as described by Bereiter et al. (2018a), with a longer equilibration time during the splitting step than used in that study to improve isotopic equilibration between the fractions. The exception is the DE08-OH site, where the ice sample (rather than the extracted gas sample) was split into two fractions – the advantage of this approach is that it does not require a gas splitting step that is time-consuming and may fractionate the isotopes; the downside is that the samples may have slightly different isotopic composition due to the stochastic nature of bubble trapping and the different gas-loss histories of the ice pieces.

Measurements of the WDC downcore data set were performed over five separate measurement campaigns that occurred in February-April 2014, February-April 2015, August 2015, August 2020, and August 2021,

244 respectively. The first three campaigns are described by Bereiter et al. (2018b), in which the $^{86}Kr_{xs}$ data are
245 a by-product of measuring $\delta Kr/N_2$ for reconstructing global mean ocean temperature. Campaigns 1 and 2
246 are in good agreement, whereas campaign 3 appears offset from the other two by an amount that exceeds
247 the analytical precision (offset around 35 per meg ‰$^{-1}$). To validate the main features in the record, we
248 performed two additional campaigns (4 and 5), in which all the gas extracted from each ice sample was
249 quantitatively gettered and only analysed for Ar and Kr isotopic composition. The downcore record, as well
250 as the five analytical campaigns, are discussed in detail in section 5.1. Data from the bubble-clathrate
251 transition zone (here 1000 to 1600 m depth, or ~4ka to 7ka BP) are excluded owing to the potential for
252 artefacts; the depth range of the bubble-clathrate transition zone is based on observed positive anomalies in
253 $\delta O_2/N_2$ in WDC ice.

254 All samples were analyzed at Scripps Institution of Oceanography, USA, with the exception of the EDC
255 samples which were analyzed at University of Bern, Switzerland (Baggenstos et al., 2019). Some of the
256 EDC samples analyzed had clear evidence of drill liquid contamination, which acts to artefactually lower
257 $^{86}Kr_{xs}$ via isobaric interference on mass 82; the late Holocene data used here were not flagged for drill liquid
258 contamination (Baggenstos et al., 2019).

259 The 2σ analytical precision of the $\delta^{15}N$, $\delta^{40}Ar$, and $\delta^{86}Kr$ measurements is around 3, 5 and 26 per meg,
260 respectively, based on the reproducibility of La Jolla Air measurements. Via standard error propagation,
261 this results in a ~ 22 per meg ‰$^{-1}$ (2σ) analytical uncertainty for both $^{86}Kr_{xs40}$ and $^{86}Kr_{xs15}$ at a site like WDC
262 where $\delta^{40}Ar \approx 1.2$ ‰. We have no true (same-depth) replicates to assess the reproducibility of $^{86}Kr_{xs}$
263 measurements experimentally. The measured isotope ratios are corrected for gas loss (Δ^{40}_{GL}) and thermal
264 fractionation ($\Delta^{86}_{TF}, \Delta^{40}_{TF}, \Delta^{15}_{TF}$) before interpretation; details on these corrections are given in appendix A.
265 For the coretop calibration study, the average magnitude of the gas loss and thermal fractionation
266 corrections is +14 and -15 per meg ‰$^{-1}$ in $^{86}Kr_{xs}$, respectively. Note that these two corrections both involve
267 the $\delta^{40}Ar$ isotopic ratio, and therefore they are not independent from each other and not additive – in other
268 words, the total correction is not simply the sum of the two individual corrections.

269 Our study includes two ice cores from the Antarctic Peninsula: BRP (2 ice samples) and JRI (5 ice samples).
270 Measured $\delta Xe/N_2$ ratios (and to a lesser extent the $\delta Kr/N_2$ ratios) in all samples from both locations are
271 significantly elevated above the expected gravitational enrichment signal (Fig. A1A), which is clear
272 evidence for the presence of refrozen meltwater in these samples (Orsi et al., 2015). Like xenon, krypton is
273 highly soluble in (melt)water, and therefore $^{86}Kr_{xs}$ cannot be reliably measured in these samples; we reject
274 all samples from the BRP and JRI sites. It is notable that all samples from both sites show evidence of
275 refrozen meltwater, given that the high-accumulation BRP core is nearly entirely free of visible melt layers,
276 and that we carefully selected samples without visible melt features at JRI. Visible ice lenses form only
277 when meltwater pools and refreezes on top of low-permeability layers such as wind crusts; our observations
278 suggest meltwater can also refreeze throughout the firn in a way that cannot be detected visually.

279

3 Calibrating Kr-86 excess

The $^{86}Kr_{xs}$ proxy for synoptic activity was first proposed on theoretical grounds by Buizert and Severinghaus (2016) – here we provide the first experimental validation of this proxy using a coretop calibration of $^{86}Kr_{xs}$ using late-Holocene ice core samples from nine locations around Antarctica and one in Greenland that represent a wide range of pressure variability in the modern climate (here: 1979-2017 CE).

3.1 Spatial variation in synoptic-scale pressure variability

Kr-86 excess is sensitive to air movement (both upward and downward), which in turn is controlled by the magnitude of relative air pressure change. Let p_i be a time series of (synoptic-scale) site surface pressure with N data points, time resolution Δt, and mean value $\bar{p}$. The time series can span a month, year, or multi-year period, with $\bar{p}$ potentially different for each month or year. We define the parameter Φ as:

$$\Phi = \frac{1}{N\bar{p}}\sum_{i=1}^{N}\left|\frac{p_i - p_{i-1}}{\Delta t}\right| \tag{5}$$

which we here express in convenient units of % day^{-1}. Φ reflects the intensity of barometric pumping in the firn column. Note that Δt should be larger than ~1 hour (, which is the timescale for the entire firn column to equilibrate with the surface pressure (Buizert and Severinghaus, 2016), and smaller than about a day (in order to adequately resolve synoptic-scale pressure events). Here we use ERA-interim reanalysis data from 1979-2017 with Δt = 6 hours (Dee et al., 2011), from which we calculate monthly and annual Φ values using Eq. (5). A map of annual-mean Φ across Antarctica is given in Fig. 2A. At all sites considered, Φ has a strong seasonal cycle with pressure variability/storminess being strongest in the local winter season (Fig. 2C). Interannual differences in Φ are greatest along the Siple coast and coastal West Antarctica (Fig. 2B), mainly reflecting the influence of central Pacific (ENSO, PDO) climate variability (Section 4).

3.2 Kr-86 excess proxy calibration

Present-day Antarctica has a wide range of Φ (Fig. 2A), which allows us to validate and calibrate $^{86}Kr_{xs}$. In Fig. 3A we plot the site mean $^{86}Kr_{xs40}$ (with $\pm 1\sigma$ error bars) as a function of Φ (averaged over full 1979-2017 period). We find a Pearson correlation coefficient of r = -0.94 when using site mean $^{86}Kr_{xs40}$, and r = -0.83 when using the $^{86}Kr_{xs40}$ of individual samples, respectively ($p < 0.01$). Note that in this particular case the site-mean $^{86}Kr_{xs40}$ and $^{86}Kr_{xs15}$ are identical (because by design, after thermal correction $\delta^{15}N = \delta^{40}Ar$); the error bars are different, though.

The $^{86}Kr_{xs}$ data have been corrected for gas loss (Appendix A1) and thermal fractionation (Appendix A2); with the gas loss correction being the more uncertain component. Figure 3B shows the correlations of the calibration curve as a function of the gas loss scaling parameter ε_{40}. We find a good correlation over a wide range of ε_{40} values, proving our calibration is not dependent on the choice of ε_{40}. When using uncorrected $^{86}Kr_{xs40}$ data the site mean correlation is r = -0.71; when applied individually, both the gas loss and thermal correction each improve the correlation to r = -0.77 and r = -0.79, respectively (Fig. A3, all $p < 0.05$). Based on these tests we conclude that the observed relationship is not an artefact of the applied corrections. The applied corrections improve the correlation, which increases confidence in the method. The calibration results for $^{86}Kr_{xs15}$ are shown in Fig. A4.

316 Notably, there is a large spread in $^{86}Kr_{xs}$ across samples from any single site, particularly at the high-Φ sites
317 of SDM and RICE (Fig. 3A, note the $\pm 1\sigma$ error bars). This spread is larger than the measurement
318 uncertainty, and we believe this variance reflects a signal that is truly present in the ice. The Siple coast and
319 Roosevelt Island experience the largest Φ interannual differences in Antarctica (Fig. 2B), and it is therefore
320 likely that our coarse sampling is aliasing the true $^{86}Kr_{xs}$ signal. The variance in $^{86}Kr_{xs}$ may contain climate
321 information also.

322 Both theoretical considerations and observations thus suggest $^{86}Kr_{xs}$ is a proxy for time-averaged barometric
323 surface pressure variability at the site, and in the remainder of this manuscript we will interpret it as such.

3.3 Discussion of the Kr-86 excess proxy

325 Our interpretation of $^{86}Kr_{xs}$ as a proxy for time-averaged pressure variability is somewhat complicated by
326 the possibility of deep convective zones, which have the same $^{86}Kr_{xs}$ signature as barometric pumping. This
327 was discovered at the Megadunes (MD) site, central East Antarctica; at this zero-accumulation site deep
328 cracks form in the firn layer that facilitate a 23 m deep convection zone (Severinghaus et al., 2010). In fact,
329 this observation led earlier work to suggest that noble gas gravitational disequilibrium may be used as a
330 proxy for convective zone thickness (Kawamura et al., 2013), rather than synoptic-scale pressure variability
331 as suggested here. Although megadunes and zero-accumulation zones are ubiquitous and cover 20% of the
332 Antarctic Plateau (Fahnestock et al., 2000), ice cores are seldom drilled in these areas and it is safe to
333 assume that they never formed at sites like WAIS Divide that had relatively high accumulation rates even
334 during the last glacial period. Performing the corrections for thermal and size-dependent fractionation is
335 challenging at MD, and we suggest that the MD $^{86}Kr_{xs}$ is in the range of -2 to -55 per meg ‰$^{-1}$; even at the
336 larger limit, this is still smaller in magnitude than $^{86}Kr_{xs}$ anomalies at several modern-day sites with small
337 convective zones (such as SDM, RICE and the Law Dome sites), suggesting barometric pumping is capable
338 of producing larger $^{86}Kr_{xs}$ signals than even the most extreme observed case of convective surface mixing.
339 Having $^{86}Kr_{xs}$ measured in MD ice core (rather than firn air) samples would be valuable for a more
340 meaningful comparison to the ice core sample measurements presented here. Windy sites can have
341 substantial convective zones of $\sim$ 14 m (Kawamura et al., 2006), and future studies of $^{86}Kr_{xs}$ at such sites
342 would be valuable.

343 Currently, 1-D and 2-D firn air transport model simulations underestimate the magnitude of the $^{86}Kr_{xs}$ signal
344 compared to measurements in mature ice samples (Birner et al., 2018), complicating scientific
345 understanding of the proxy. In these models, the effective molecular diffusivity of each gas is scaled linearly
346 to its free air diffusivity. The ratio of krypton to argon free air diffusivity is 0.78. This ratio, which directly
347 sets the magnitude of the simulated $^{86}Kr_{xs}$, may actually be smaller than 0.78 in real firn, as krypton is more
348 readily adsorbed onto firn surfaces retarding its movement (similar to gasses moving through a gas
349 chromatography column). This may be one explanation for why models simulate too little $^{86}Kr_{xs}$.

350 Another likely explanation for the model-data mismatch is that certain critical sub-grid processes (such as
351 the aforementioned pore-size dependence of the Péclet number) are not adequately represented in these
352 models. Barometric pumping may further actively shape the pore network through the movement of water
353 vapor, thereby keeping certain preferred pathways connected and open below the density where percolation
354 theory would predict their closure (Schaller et al., 2017). The fate of a pore restriction is determined by the
355 balance between the hydrostatic pressure (that acts to close it) and vapor movement away from its convex

356   surfaces (that acts to keep it open); we speculate that barometric Darcy air flow keeps high-flow channels
357   connected longer by eroding convex surfaces. This enhances the complexity (and therefore dispersivity) of
358   the deep firn pore network and possibly creates a non-linear $^{86}Kr_{xs}$ response to barometric pumping. The
359   hypothesized channel formation in deep firn is driven by a positive feedback on flow volume, and somewhat
360   reminiscent of erosion-driven stream network formation in fluvial geomorphology.

361   Firn models predict that, after correcting for thermal fractionation, the deviation from gravitational
362   equilibrium for the elemental ratios (such as $\delta Kr/Ar$) should be proportional to that deviation in isotopic
363   ratios. However, the observations suggest that the former is usually smaller than would be expected from
364   the latter. As before, adsorption of Kr onto firn grain surfaces may contribute to the observed discrepancy,
365   and laboratory tests of this process are called for. Further, the impacts of gas loss are greater on elemental
366   ratios than on the isotopic ratios which may contribute also. Including measurements of xenon isotopes and
367   elemental ratios in future measurement campaigns may be able to provide additional constraints to better
368   understand this discrepancy.

369   Measurements on firn air samples, where available, suggest a smaller $^{86}Kr_{xs}$ anomaly in firn air than found
370   in ice core samples from the same site. We attribute this in part to a seasonal bias that is introduced by the
371   fact that firn air sampling always takes place during the summer months, whereas the synoptic variability
372   that drives the Kr-86 excess anomalies is largest during the winter (Fig. 2C); consequently, firn air
373   observations are biased towards weaker $^{86}Kr_{xs}$. Further, in the deep firn where $^{86}Kr_{xs}$ anomalies are largest,
374   firn air pumping may not yield a representative air sample, but rather be biased towards the well-connected
375   porosity at the expense of poorly-connected cul-de-sac-like pore clusters. Since barometric pumping
376   ventilates this well-connected porespace with low-$^{86}Kr_{xs}$ air from shallower depths, the firn air sampling
377   may not capture a representative $^{86}Kr_{xs}$ value of the full firn air content. These explanations are all somewhat
378   speculative, and a definitive understanding of the firn-ice differences is lacking at this stage.

379   Gas loss and thermal corrections are critical to the interpretation of $^{86}Kr_{xs}$. The thermal correction is applied
380   to account for thermal gradients in the firn (ΔT, here defined as the temperature at the top minus the
381   temperature at the base of the firn), which are chiefly caused by geothermal heat or surface temperature
382   changes at the site. At low-accumulation sites geothermal heating leads to $\Delta T < 0$. We use ^{15}N-excess ($\delta^{15}N$
383   $- \delta^{40}Ar/4$) to estimate the thermal gradient in the firn (Appendix A2). Because nitrogen and argon have
384   similar diffusivities but different thermal diffusion coefficients, $\delta^{15}N - \delta^{40}Ar$ is relatively insensitive to
385   barometric pumping yet sensitive to thermal fractionation, allowing estimating ΔT.

386   Besides the actual thermal gradients in the firn, the isotopic composition may also be impacted by seasonal
387   rectifier effects. If the firn air transport properties differ between the seasons (for example due to thermal
388   contraction cracks, convective instabilities, or seasonality in wind pumping), this can result in a thermal
389   fractionation of isotopic ratios in the absence of a thermal gradient ΔT in mean annual temperature (Morgan
390   et al., 2022).

391   For the WDC, DSS and GISP2 sites we obtain ΔT values close to zero as expected for these high-
392   accumulation sites; for the SP, SDM, RICE, and DF sites we find ΔT ranging from -0.76 to -1.18°C, in
393   agreement with the effect of geothermal heat. The high-accumulation DE08 and DE08-OH sites both have
394   an unexpectedly large ΔT of -1.6°C; the good agreement between the sites suggest it is likely a real signal,

395   yet we can rule out geothermal heat as the cause. This may suggest that the Law Dome DE08 site is subject
396   to a seasonal rectifier effect, or a recent climatic cooling. Last, the EDC site shows an unexpected positive
397    $\Delta T = +1.6 \pm 1.89°C$. Three possible explanations are: (1) the aforementioned drill liquid contamination for
398   this core (Baggenstos et al., 2019); (2) a summertime-biased seasonal rectifier; or (3) an over-correction of
399    $\delta^{40}Ar$ for gas loss, which could occur for example if natural and post-coring fugitive gas loss fractionate
400    $\delta^{40}Ar$ differently and EDC samples were impacted mostly by the former type (our correction is mostly
401   based on measurements of the latter type).

402   For the Law Dome DE08-OH site we observe large (5-fold) sub-annual variations in $^{86}Kr_{xs}$ (Fig. B1). The
403   magnitude of the $^{86}Kr_{xs}$ layering is truly remarkable. The isotopic enrichment of each gas ($\delta^{15}N$, $\delta^{40}Ar$,
404    $\delta^{86}Kr$) can be converted to an effective diffusive column height (DCH). For the samples with the smallest
405   (greatest) $^{86}Kr_{xs}$ magnitude, this DCH is around 1 m (6 m) shorter for $\delta^{86}Kr$ than it is for $\delta^{15}N$. The firn air
406   transport physics that may explain such phenomena are beyond our current scientific understanding. The
407   sub-annual variations may be related to the seasonal cycle in storminess, though that seems improbable to
408   us at present as the gas age distribution at the depth of bubble closure has a width of several years
409   (Schwander et al., 1993). Another reason may be seasonal layering in firn properties – such as density,
410   grain size, and pore connectivity – that control the degree of disorder and dispersive mixing occurring in
411   the firn, and lead to a staggered firn trapping and seasonal variations in Δage (Etheridge et al., 1992; Rhodes
412   et al., 2016). The sample air content estimated from the IRMS inlet pressure is similar for all measurements,
413   making it unlikely that the variations in $^{86}Kr_{xs}$ are caused by remnant open porosity in lower-density layers.
414   In any case it is remarkable that such large variations in gas composition can arise and persist on such small
415   length scales, given the relatively large diffusive, dispersive, and advective transport length scales of the
416   system. More work is needed to establish the origin of the sub-annual variations in ice core $^{86}Kr_{xs}$. At all
417   other sites analyzed here, the sample length exceeds the annual layer thickness; this will remove some, but
418   not all, of the effects of the sub-annual variations.

419   Another puzzling observation is the positive $^{86}Kr_{xs}$ at the Dome Fuji (DF) site; theoretical considerations
420   suggest it should always be negative. In part this may be due to an over-correction of $\delta^{40}Ar$ for gas loss,
421   which would act to bias $^{86}Kr_{xs}$ in the positive direction. This correction is largest at DF owing to the very
422   negative $\delta O_2/N_2$ and $\delta Ar/N_2$ (Fig. A1); while we base our correction on published work, it is conceivable
423   that we overestimate the true correction (Appendix A1). In particular, our gas loss correction is based on
424   observations on artefactual post-coring gas loss, which may fractionate $\delta^{40}Ar$ differently than natural
425   fugitive gas loss during bubble close-off. Omitting the gas loss correction indeed makes $^{86}Kr_{xs}$ at DF
426   negative (Fig. A3C-D). Another hypothesis is that the positive $^{86}Kr_{xs}$ signal is an artefact of the seasonal
427   rectifier that Morgan et al. (2022) identify at DF. In this work we assume a linear approach in which the
428   effect of the rectifier can be described by a single ΔT value that is the same for isotopic pairs. In reality,
429   there may be non-linear interactions between thermal fractionation and firn advection that impact the
430   isotopic values of the various gases in a more complex way than captured in our approach.

431   The $^{86}Kr_{xs}$ is also correlated with other site characteristics besides Φ. For site elevation we find $r = 0.96$
432   (0.84); and for mean annual temperature $r = -0.87$ (-0.76); the number in parentheses gives the correlation
433   when using all the individual samples rather than site-mean $^{86}Kr_{xs}$. The listed correlations all have $p < 0.01$.
434   For site accumulation we do not find a statistically significant correlation at the 90% confidence level. The
435   correlations with elevation and temperature are comparable to those we find for Φ; this is no surprise given

that elevation, Φ and T are all strongly correlated with one another, mainly because elevation directly impacts both T (via the lapse rate) and Φ (via its topographic influence on the position of storm tracks). To our knowledge there are no mechanisms through which either elevation or annual-mean temperature could drive kinetic isotopic fractionation in the firn layer. Perhaps other unexamined site characteristics (such as the degree of density layering, or the magnitude of the annual temperature cycle) could provide good correlations also, suggesting additional hidden controls on $^{86}Kr_{xs}$. The data needed to assess such hidden controls are not available for most sites.

The calibration of the $^{86}Kr_{xs}$ proxy is based on spatial regression. In applying the proxy relationship to temporal records, we make the implicit assumption that proxy behavior in the temporal and spatial dimensions is at least qualitatively similar. This assumption may prove incorrect. In particular, changes in insolation are known to impact firn microstructure and bubble close-off characteristics, which in turn impacts gas records of $\delta O_2/N_2$ and total air content (Bender, 2002; Raynaud et al., 2007). Since $^{86}Kr_{xs}$ is linked to the dispersivity of deep firn, it seems probable that insolation has a direct impact on $^{86}Kr_{xs}$ also via the firn microstructure. We will revisit this issue in our interpretation of the WDC $^{86}Kr_{xs}$ record (Section 5). Overall, we anticipate $^{86}Kr_{xs}$ to be a qualitative proxy for synoptic variability, yet want to caution against quantitative interpretation based on the spatial regression slope.

The observations presented in this section clearly highlight the fundamental shortcomings of our current understanding of firn air transport hinting at the existence of complex interactions, presumably at the pore-scale, that are not being represented. Percolation theory finds that near the critical point (presumably the lock-in depth) a network becomes fractal in its nature; we suggest that this fractal nature of the pore network likely contributes to non-linear pore-scale interactions that give rise to the $^{86}Kr_{xs}$ observations in ice. While the observed correlation of Fig. 3A is highly encouraging, further work is critical to understand this proxy. Examples of such future studies are: (1) additional high-resolution records that can resolve the true variations that exist in a single ice core, similar to the DE08-OH record; (2) 3-D firn air transport model studies; (3) improvements to the gas loss correction; (4) additional coring sites to extend the spatial calibration and further confirm the validity of the proxy; (5) Adding xenon isotopic constraints (^{136}Xe excess) as an additional marker of isotopic disequilibrium; (6) numerical simulations of pore-scale air transport in large-scale firn networks; (7) experimental studies of dispersion and noble gas adsorption in firn samples; (8) percolation theory approaches to study the fractal nature of the pore network of the lock-in zone; and (9) replication of the WDC deglacial $^{86}Kr_{xs}$ record in nearby ice cores such as RICE.

4 Present-day controls on Kr-86 excess in Antarctica

In this section we investigate the large-scale patterns of climate variability in the Southern Hemisphere that could affect Φ and therefore $^{86}Kr_{xs}$ over Antarctica. We begin by investigating the patterns in the wind field that are associated with changes in Φ at ice core sites, before examining how more canonical patterns of Southern Hemisphere climate variability, such as the southern annular mode (SAM), might affect Φ over the whole of Antarctica.

We use ERA-interim reanalysis data for the 1979-2017 period (Dee et al., 2011) to evaluate the present-day controls on synoptic-scale pressure variability in Antarctica. Kr-86 excess in an ice core sample averages over several years of pressure variability, and therefore we focus on annual-mean correlation in our analysis. The annual-mean Φ is calculated from the 6-hourly reanalysis data using Eq. (5). Note that we let the year run from April to March to avoid dividing single El Niño / La Niña events across multiple years.

At all Antarctic sites investigated, a similar pattern exists; four representative locations are shown in Fig. 4, where we regress the zonal wind in the lower (850 hPa, color shading) and upper troposphere (200 hPa, contours) onto our surface pressure variability parameter Φ. We find that synoptic pressure variability at these sites is linked to zonal winds along the southern margin of the eddy-driven subpolar jet (SPJ), which extends from the surface to the upper troposphere (Nakamura and Shimpo, 2004; Trenberth, 1991). Sites near the ice sheet margin (Figs. 4A, B and D) are most sensitive to the SPJ edge in their sector of Antarctica, whereas interior sites (Fig. 4C) appear sensitive to the overall strength/position of the SPJ. Note that strengthening, broadening or southward shifting of the SPJ all can in principle enhance site Φ.

Pressure variability at WDC is furthermore correlated with the strength of the Pacific Subtropical jet (STJ) aloft (solid contour lines centered around 30ºS in the Pacific in panel 4A), forming an upper troposphere wind pattern that resembles the wintertime South Pacific split jet (Bals-Elsholz et al., 2001; Nakamura and Shimpo, 2004); this agrees with the finding that a strengthening of the split jet enhances storminess over West Antarctica (Chiang et al., 2014).

Next, we investigate how the well-known patterns of large-scale atmospheric variability, such as SAM and ENSO, impact pressure variability in Antarctica. Figure 5 shows the correlation of Φ with the three leading modes of SH extra-tropical atmospheric variability; the correlation with various indices and modes for individual ice core locations is given in Table 2. Most teleconnection patterns have a specific season during which they are strongest; here we do not differentiate between seasons, because $^{86}Kr_{xs}$ in ice core samples averages over all seasons.

Globally, annual-mean Φ is highest over the Southern Ocean (Fig. 5A); a region of enhanced baroclinicity associated with the eddy-driven SPJ (Nakamura and Shimpo, 2004). The green line denotes the latitude of maximum Φ, corresponding roughly to the latitude with the highest storm track density (57.8ºS on average).

The dominant mode of atmospheric variability in the SH extratropics is the southern annular mode, representing the vacillation of atmospheric mass between the mid- and high-latitudes (Thompson and Wallace, 2000). Figure 5B shows 500 hPa geopotential height (Z500) anomalies associated with the SAM as contours, with the color shading giving the correlation between Φ and the SAM index. During the

positive SAM phase (negative Z500 over Antarctica) we find that the stormtracks and maximum synoptic activity are displaced towards Antarctica (positive Φ correlation poleward of the green line in Fig. 5B). This is associated with a strengthening and poleward displacement of the SH westerly winds that occurs during a positive SAM phase. More locally, Φ on the Antarctic Peninsula is positively correlated with the SAM-index (Table 2); Φ at the other sites is not meaningfully impacted. This suggests that the variations associated with the SAM (as commonly defined) do not extend far enough poleward to meaningfully impact Antarctica with the exception of the Peninsula. Enhanced synoptic variability on the Peninsula during positive SAM phases is consistent with observations of enhanced snowfall at those times (Thomas et al., 2008).

The second mode of SH extratropical variability is the Pacific-South American Mode 1 (PSA1), which reflects a Rossby wave response to sea surface temperature (SST) anomalies over the central and eastern equatorial Pacific (Mo and Paegle, 2001), and is therefore closely linked to ENSO on interannual time scales (we find a correlation of $r = 0.77$ between the annual mean PSA1 and Niño 3.4 indices). Φ in the Amundsen and Ross Sea sectors (WDC, SDM and RICE) is positively correlated to the PSA1 and Niño 3.4 SST, suggesting larger synoptic activity during El Niño phases and low activity during La Niña phases. The PSA2 pattern, also linked to SST anomalies in the tropical Pacific (Mo and Paegle, 2001), is likewise correlated to Φ in the Amundsen and Ross Sea sectors (Fig. 5C and Table 2). While all the correlations listed are statistically significant, they explain only a fraction of the total variability.

Next, we consider anomalies in sea ice area and extent (Parkinson and Cavalieri, 2012). We focus on the Ross and Amundsen-Bellishausen Seas where impacts on WAIS Divide may be expected. At the 90% confidence level we do not find significant correlations to sea ice area or extent at most core locations (Table 2). Correlations to sea ice extent are (even) weaker than those for sea ice area and consequently not shown. We performed a lead-lag study of the correlations between Φ and sea ice area/extent in the various sectors, and find that in all cases maximum correlations occur for the sea ice changes lagging 0 to 4 months behind Φ; we interpret this to mean that the sea ice is responding to changes in atmospheric circulation, rather than driving them.

Overall, we find that synoptic activity at WAIS Divide, the site of most interest here, is controlled by the position and/or strength of the stormtracks at the southern edge of the SPJ in the Pacific sector of the Southern Ocean (Ross, Amundsen and Bellishausen Seas), with little sensitivity to the SPJ behavior in the other sectors. Owing to its remote southern location, WDC is only weakly impacted by the commonly-defined large-scale modes of atmospheric variability. Most notably, WDC has a modest influence from the tropical Pacific climate, as shown by a correlation around $r \approx 0.3$ to the PSA1, Niño 3.4 and PDO indices (Table 2). We further find statistically significant correlations (up to $r = 0.44$) between WDC Φ and SST in broad regions of the central and eastern tropical Pacific (not shown). We suggest that ENSO weakly impacts storminess at WDC (around 10% of variance explained) via its impact on the SPJ in the South Pacific.

5 Barometric variability in West Antarctica during the last deglaciation

5.1 The 0-24 ka WAIS Divide Kr-86 excess record

The WAIS Divide downcore ^{86}Kr$_{xs}$ dataset we present here was produced during five separate measurement campaigns that occurred in February-April 2014, February-April 2015, August 2015, August 2020, and August 2021, respectively. Campaigns 1-3 were reported previously (Bereiter et al., 2018a; Bereiter et al., 2018b), and campaigns 4 and 5 were meant to resolve conflicts between the ^{86}Kr$_{xs}$ data sets from these earlier campaigns. Three slightly different measurement approaches were used. Campaign 1 uses "Method 1" from Bereiter et al. (2018a), in which the air sample splitting is done in a water bath for over 12 hours to equilibrate the sample. Campaigns 2 and 3 use "Method 2" from Bereiter et al. (2018a), in which a bellows is used to split the air samples for over 4 to 6 hours. Campaigns 4 and 5 do not involve splitting of the air sample, and only analyzed the Kr and Ar isotopic ratios. During campaign 4 a glass bead from the water trap had gotten stuck in the tubing, restricting the flow and likely resulting in incomplete air extraction from the melt water.

Figure 6 compares ^{86}Kr$_{xs40}$ (panel A) and ^{86}Kr$_{xs15}$ (panel B) from the five campaigns. Campaign 1 is the only campaign that spans the full age range of the record, making it the most valuable of the three campaigns. Campaigns 2 and 3 are mostly restricted to the Pleistocene and Holocene periods respectively, with little overlap between them. Campaigns 4 and 5 aimed to reproduce some of the most salient features in the earlier three. For ease of visual comparison, a Gaussian smoothing spline to the combined data from the two most extensive campaigns (1 and 2) is added (details below).

Visual inspection suggests that campaigns 1 and 2 agree well for both ^{86}Kr$_{xs}$ definitions; campaign 3 has more scatter and is visibly offset (more negative) for both ^{86}Kr$_{xs}$ definitions; campaign 4 has several data points that agree well with the spline, yet also several fliers with very negative ^{86}Kr$_{xs40}$; campaign 5 appears overall more negative in ^{86}Kr$_{xs40}$. No true replicate samples were analyzed between the campaigns, in part because the large sample size requirement precludes this. ~~To assess~~ This precludes a direct assessment of campaign offsets~~,~~. Instead we rely on ~~nearest neighbor~~ linear interpolation. ~~We find an offset of 5 per meg between~~ First, we linear interpolate the ~~first~~ ^{86}Kr$_{xs}$ values of campaign 1 onto the sample depths of campaign 2, and ~~second campaign (~~ vice versa, allowing us to estimate the offsets. In this way, ~~during their period of overlap); this~~ we estimate offsets of 6 and 13 per meg ‰$^{-1}$ between campaigns 1 and 2 for ^{86}Kr$_{xs40}$ and ^{86}Kr$_{xs15}$, respectively. This is within the analytical precision (22 per meg), suggesting these two campaigns are in good agreement. ~~The agreement is good for both the ^{86}Kr$_{xs40}$ and ^{86}Kr$_{xs15}$ definitions. The first downcore campaign furthermore overlaps in depth with the WDC calibration dataset (gray data in Fig. 6); we find no offset between those data sets either.~~ Data from campaign 2 appear to have more scatter, possibly reflecting the shorter equilibration time during sample splitting.

We combine data from the first two campaigns, and evaluate their offset to data from the other three campaigns again using ~~nearest neighbor~~ the linear interpolation method. For campaigns 3, 4 and 5 we find an offset of ~~-31,~~ 32, -22 and -23 per meg ‰$^{-1}$ in ^{86}Kr$_{xs40}$, respectively. For campaign 3 the offset is -34 per meg ‰$^{-1}$ in ^{86}Kr$_{xs15}$. It is remarkable that all three later campaigns are more negative in ^{86}Kr$_{xs}$ than the first two. Campaign 3 shows the greatest offset (greater than analytical precision), and has more scatter in both ^{86}Kr$_{xs}$ (Fig. 6) and ^{15}N excess ~~(Fig. A5), and,~~ possibly because for this campaign less care was taken ~~during this campaign~~ that

580 the IRMS conditions were stable. The offset of campaign 4 may be attributed to the incomplete sample
581 transfer due to the bead stuck in the line~~.~~; note that for this campaign the offset is caused by two very
582 negative data points. The offset in campaign 5 is hard to explain. The ~~systematically~~ more negative $^{86}Kr_{xs}$
583 of campaigns 4 and 5 may reflect sample storage effects, as these were measured 5-6 years after campaign
584 1 and 2. However this would not explain the negative values of campaign 3. The good $^{86}Kr_{xs}$ agreement
585 between DE08 and DE08-OH, drilled 32 years apart, would also argue against large storage effects. For
586 campaign 4 and 5 only Ar and Kr isotope ratios were measured, and so we lack typical tracers of gas loss
587 ($\delta O_2/N_2$ and $\delta Ar/N_2$~~.)~~) that can be analyzed.

588 In the remainder of this paper we will interpret the combined data from campaigns 1 and 2, but with the
589 caveat that there is a persistent offset with later campaigns. However, the features we interpret are
590 corroborated by the later campaigns, if one takes the offset into account. To aid interpretation of the data,
591 we apply a Gaussian smoothing spline with a smoothing filter width that varies depending on the data
592 density (from 250-year width in the deglaciation itself where the data density is high, to 1750 years in the
593 Holocene and LGM where data density is low). To estimate the uncertainty in the smoothing spline we use
594 a Monte Carlo approach that considers uncertainty in (1) the gas loss correction, by randomly sampling ε_{40}
595 in the range of 0 to -0.~~008;~~016, and by randomly adding an offset in the range of -1‰ to +1‰ to the gas
596 loss indicator ($\delta O_2/N_2 - \delta Ar/N_2$); (2) the thermal correction, by randomly scaling the thermal scenario (Fig.
597 A5) by a factor ranging from 0 to 2; and (3) analytical errors, by adding random errors to individual data
598 points drawn from a normal distribution with a 2σ width of 22 per meg. The $\pm 1\sigma$ uncertainty range with
599 mean value are shown as the gray envelope and center line in Fig. 6. We believe the following observations
600 to be robust:

601 • The Holocene shows a trend towards increasingly negative $^{86}Kr_{xs}$, suggesting a gradual increase in
602 synoptic activity toward the present. Minimum synoptic activity in West Antarctica occurs during the
603 early Holocene around 10 ka BP; the Monte Carlo study suggests $^{86}Kr_{xs40}$ in the early Holocene (8ka-
604 10ka BP) is 30.5 ±18 per meg ‰$^{-1}$ ($\pm 2\sigma$) below the late-Holocene value (last 2 ka). Using the slope of
605 our core-top calibration (Fig. 3), we estimate that early-Holocene WDC synoptic activity Φ is ~17%
606 weaker than it is today. This change is comparable to the 2σ magnitude of interannual variations in
607 annual mean Φ at the site today (or about half the peak-to-peak variations thereof). This Holocene trend
608 is seen in the data from campaigns 1, 3 and 4. Campaign 5 does not suggest a trend but has only one
609 late Holocene data point making it less robust. The trend in campaign 3 is less robust due to the greater
610 scatter in the data.
611 • The most pronounced change occurs at the Younger Dryas (YD) - Holocene transition, where $^{86}Kr_{xs}$
612 becomes more positive (by 30.1 ±16 per meg ‰$^{-1}$, comparing YD and early Holocene) implying a
613 decrease in synoptic activity. This transition is observed in campaigns 1, 2, 4 and 5 that cover this time
614 period (the third campaign does not cover it), and represents a ~17% drop in synoptic activity (Φ).
615 • During the Last Glacial Maximum (LGM), WDC synoptic activity was perhaps slightly weaker than at
616 present, but not significantly so ($^{86}Kr_{xs40}$ more positive by 11 ±13 per meg ‰$^{-1}$). The West Antarctic
617 ice sheet elevation was likely higher during the LGM, and a 300 m elevation increase would by itself
618 increase $^{86}Kr_{xs40}$ by 10 per meg ‰$^{-1}$, all else being equal (Appendix A3); this is within the analytical
619 error of our observations. This feature is seen in campaign 1 and not covered by the other campaigns.
620 • The deglaciation itself has enhanced synoptic activity, in particular during the two North-Atlantic cold
621 stages Heinrich Stadial 1 (HS1) and the YD as highlighted with yellow bars in Figs. 6 and 7. Synoptic

622   activity during these periods is enhanced relative to the adjacent LGM and early Holocene, yet
623   comparable to today. This feature is seen in campaigns 1 and 2, and in 4 and 5 for the transition into
624   the Holocene.

625 Below we will interpret the deglacial WDC ^{86}Kr$_{xs}$ record in terms of time-averaged barometric variability.
626 Before doing so we want to emphasize that firn processes may have been imprinted onto the record also, in
627 particular on orbital timescales where firn microstructure responds to local (summer) insolation intensity
628 (Bender, 2002). High summer insolation results in more depleted $\delta O_2/N_2$ and reduced air content, likely via
629 stronger layering and a delayed pore close-off process (Fujita et al., 2009).

630 Local summer solstice insolation in Antarctica increases through the Holocene, with the highest values in
631 the late Holocene. This may impact ^{86}Kr$_{xs}$, although it is not a-priori clear what the sign of this relationship
632 would be. The sense of the Holocene temporal trends is that a more negative ^{86}Kr$_{xs}$ coincides with more
633 negative $\delta O_2/N_2$. Note that this is opposite to the trends seen in the spatial calibration, where sites with the
634 most negative $\delta O_2/N_2$ (DF, SP, EDC) have the most positive ^{86}Kr$_{xs}$. For now, the impact of local insolation
635 on ^{86}Kr$_{xs}$ via firn microstructure remains unknown, which is an important caveat in interpreting the orbital-
636 scale changes in WDC ^{86}Kr$_{xs}$. The abrupt ^{86}Kr$_{xs}$ increase at the Holocene onset is too abrupt to be caused by
637 insolation changes, and thus we can interpret that change with more confidence.

638 The scatter in the late Holocene WDC ^{86}Kr$_{xs}$ data exceeds the stated analytical precision. Potential
639 explanations include (1) an underestimation of the true analytical precision; (2) interannual to decadal
640 variations in storminess at WDC; and (3) aliasing of cm-scale variations in ice core ^{86}Kr$_{xs}$ linked to layering
641 in firn microstructural properties. Understanding the cause of this relatively high scatter in the ^{86}Kr$_{xs}$ records
642 will require more work, in particular the measurements of several high resolution ^{86}Kr$_{xs}$ records in various
643 sectors of Antarctica.

5.2 Barometric variability at WAIS Divide during the last deglaciation

645 In the present-day, synoptic-scale pressure variability at WAIS Divide is correlated with zonal wind
646 strength along the southern margin of the SPJ (Section 4). In our interpretation, a more negative ^{86}Kr$_{xs}$
647 reflects a strengthening or southward shift of the SPJ in the Pacific sector. Here we provide a climatic
648 interpretation of the deglacial WDC ^{86}Kr$_{xs}$ record, and suggest that variations in synoptic variability at WDC
649 are linked to meridional movement of the ITCZ on millennial and orbital timescales.

650 The main features of the deglacial WDC ^{86}Kr$_{xs}$ record listed in Section 5.1 resemble similar features seen
651 in records of (sub-) tropical hydrology and monsoon strength, such as the speleothem calcite δ^{18}O records
652 from Hulu Cave, China (Fig. 7C) and from Botuvera cave, southern Brazil (Fig. 7D), which are thought to
653 reflect the intensity of the East Asian and South American summer monsoons, respectively (Cruz et al.,
654 2005; Wang et al., 2007; Wang et al., 2001). These two monsoon records are anti-correlated, showing
655 opposing rainfall trends between the NH and SH on both orbital and millennial timescales. This pattern is
656 commonly attributed to displacement of the mean meridional position of the ITCZ (Chiang and Friedman,
657 2012; McGee et al., 2014; Schneider et al., 2014), driven by hemispheric temperature differences (Fig. 7B).
658 On orbital timescales such ITCZ migration has a strong precessional component, moving towards the
659 hemisphere with more intense summer peak insolation; on millennial timescales the ITCZ responds to
660 abrupt North-Atlantic climate change associated with the D-O and Heinrich cycles (Broccoli et al., 2006;

661 Chiang and Bitz, 2005; Wang et al., 2001), which are in turn linked to changes in meridional heat transport
662 by the Atlantic meridional overturning circulation, or AMOC (Lynch-Stieglitz, 2017; Rahmstorf, 2002).

663 Changes in mean ITCZ position have a strong influence on the structure and strength of the SH jets. During
664 periods when the NH is relatively cold (such as D-O stadials or periods with negative orbital precession
665 index) the ITCZ is displaced southward and the SH Hadley cell is weakened, thereby also weakening the
666 SH upper-tropospheric subtropical jet (Ceppi et al., 2013; Chiang et al., 2014). The reverse is also true, with
667 the ITCZ shifted northward during NH warmth, associated with a strengthening of the SH Hadley cell and
668 STJ. In a range of model simulations (Ceppi et al., 2013; Lee and Kim, 2003; Lee et al., 2011; Pedro et al.,
669 2018) the weakening of the SH STJ (as during NH cold) is furthermore accompanied by a strengthening
670 and/or southward shift of the SPJ/eddy-driven jet and SH westerly winds. Recently, ice core observations
671 have confirmed in-phase shifts in the position of the SHW occur during the D-O cycle in parallel to those
672 of the ITCZ (Buizert et al., 2018; Markle et al., 2017). Marine records of fluvial sediment runoff off the
673 Chilean coast suggest precession-phased movement of the South Pacific SPJ, again in parallel to the ITCZ
674 movement (Lamy et al., 2019).

675 The SAM index reflects the meridional position of the SHW and eddy-driven jet. During positive SAM
676 phases the SHW are displaced poleward, and during negative phases equatorward. Present-day month-to-
677 month changes in SAM index represent a mode of internal variability, with anomalies persisting for only
678 weeks to months – the timescale is longest in late spring and early summer reflecting a stronger planetary
679 wave–mean flow interaction (Simpson et al., 2011; Thompson and Wallace, 2000). By contrast, shifts in
680 the ITCZ and SH jet structure on millennial and orbital timescales have a much longer lifetime and different
681 dynamics, being driven from the tropics via hemispherically asymmetric changes in Hadley cell and STJ
682 strength. Therefore, present-day SAM internal variability is not expected to be a good analogue for past
683 changes in SHW position. We find that the present-day SAM month-to-month internal variability mainly
684 impacts synoptic variability over the Southern Ocean and does not have a statistically significant impact at
685 WDC (Table 2). Such variability is likely to have occurred during other climatic regimes also, possibly just
686 centered around a mean SHW position that is displaced meridionally relative to today. At first glance it
687 may appear contradictory to state, as we do, that synoptic activity at WDC is not sensitive to the SAM while
688 also suggesting that during the last deglaciation synoptic activity at WDC is linked to changes in the position
689 of the SH eddy-driven jet and westerlies. Based on the considerations above, both claims may be true
690 without contradiction.

691 Besides secular changes to the SPJ position/strength linked to meridional ITCZ movement, WDC $^{86}Kr_{xs}$
692 may also have imprints from ENSO and tropical Pacific climate. Our analysis suggests a weak, but
693 statistically significant link to common ENSO indicators (Table 2). Increased synoptic activity at WDC is
694 linked to enhanced convection in the central and eastern tropical Pacific, which may be due to enhanced
695 frequency or intensity of El Niño events, or a mean climate state that is more El Niño-like; it seems likely
696 that the Pacific mean state and ENSO variability are strongly linked (Salau et al., 2012), and the distinction
697 may be irrelevant.

698 The key features of the WDC $^{86}Kr_{xs}$ record are compatible with paleo-ENSO changes commonly described
699 in the literature. A majority of Holocene ENSO reconstructions (Conroy et al., 2008; Driscoll et al., 2014;
700 Koutavas et al., 2006; Moy et al., 2002; Riedinger et al., 2002; Sadekov et al., 2013) and a wide range of
701 climate model simulations (Braconnot et al., 2012; Cane, 2005; Clement et al., 2000; Liu et al., 2000; Liu

702 et al., 2014; Zheng et al., 2008) all suggest weakened ENSO activity during the early and mid-Holocene, a
703 time with reduced WDC synoptic activity. For example, Fig. 7F shows the number of El Niño events per
704 century (with trend line) reconstructed from inorganic clastic laminae in sediments from Laguna
705 Pallcacocha, Ecuador, a region strongly affected by ENSO (Moy et al., 2002). Likewise, it has been
706 suggested that the SST gradient between the West Pacific warm pool and East Pacific cold tongue was
707 enhanced during the mid-Holocene, perhaps indicating a more La Niña-like mean climate state (Koutavas
708 et al., 2002; Sadekov et al., 2013).

709 Going from the early Holocene to the Younger Dryas (YD), we observe a large increase in WDC synoptic
710 activity. Enhanced ENSO activity during Heinrich stadials is generally supported by climate model
711 simulations (Braconnot et al., 2012; Merkel et al., 2010; Timmermann et al., 2007), and by limited proxy
712 evidence for stadial periods more broadly (Stott et al., 2002). Enhanced ENSO variability during the
713 deglaciation is also found by Sadekov et al. (2013), although their record lacks the temporal resolution to
714 resolve the individual stages. The zonal SST gradient in the equatorial Pacific further reaches a minimum
715 during HS1, also consistent with higher El Niño intensity (Sadekov et al., 2013).

716 The observed variations in $^{86}Kr_{xs}$ and implied changes in WDC synoptic activity may thus have two
717 contributions: (1) ITCZ-driven changes to the South Pacific SPJ position, and (2) changes to ENSO activity.
718 Based on previous work, we argue these two amplify one another in driving WDC storminess, yet we expect
719 the former to make the larger contribution. To disentangle zonally-uniform changes to the SPJ from changes
720 specific to the Pacific sector (such as ENSO and the split jet), $^{86}Kr_{xs}$ records from different sectors of
721 Antarctica are needed. Replication of the deglacial and Holocene WDC $^{86}Kr_{xs}$ record presented here is also
722 a high priority, both at WDC itself and at the nearby SDM and RICE cores, to validate that the signals we
723 describe and interpret here are indeed real and regional in scale.

724 The position of the SHW during the LGM has been a topic of much scientific inquiry. Proxy data have been
725 interpreted to show a northward LGM shift of the SHW – with other scenarios, including no change at all,
726 not excluded by the data (Kohfeld et al., 2013). Such a shift is not supported by most climate models (Rojas
727 et al., 2009; Sime et al., 2013). Our $^{86}Kr_{xs}$ record suggests LGM synoptic activity in West Antarctica to be
728 comparable to today after accounting for site elevation effects (the elevation effect on $^{86}Kr_{xs}$ is within the
729 analytical error). This would be consistent with a Pacific SPJ position similar to today. Note that our site is
730 mostly sensitive to the position of the southern edge of the SPJ, and cannot meaningfully constrain changes
731 to the seasonality, width, and/or northern edge of the stormtracks. Therefore, it is not a-priori clear whether
732 our observations can be extrapolated to more general statements about SHW position and strength during
733 the LGM. Our data suggest that SPJ movement follows insolation and the ITCZ position, and hence the
734 LGM period may not be a good target for studying SHW movement in the first place given that it has a
735 precession index similar to the present-day.

736 Changes to the SPJ and its associated westerly surface winds have implications for ocean circulation and
737 marine productivity in the Southern Ocean via wind-driven upwelling. Opal flux records from the Antarctic
738 zone (Fig. 7G), reflecting diatom productivity, are commonly interpreted as a proxy for such upwelling –
739 with enhanced upwelling during southward displacement of the SHW (Anderson et al., 2009). Here we
740 only show records from the Pacific sector, given we find WDC $^{86}Kr_{xs}$ to reflect purely local SPJ dynamics
741 (Fig. 4A). Both published records suggest enhanced upwelling during the deglaciation (Fig. 7G), consistent
742 with a southward-shifted Pacific SPJ and enhanced storminess at WDC. The record from core PS75/072-4

743   (blue curve) further indicates an increasing productivity trend through the Holocene (Studer et al., 2018),
744   which is accompanied by a rise in surface nitrogen availability (reconstructed from diatom-bound nitrogen
745   isotopic composition, not shown); this Holocene trend matches our finding of increasing WDC storminess
746   and, by inference, an increasingly southern position of the Pacific SPJ and SHW. We thus conclude that
747   our interpretation of WDC $^{86}Kr_{xs}$ reflecting SPJ movement in parallel with the ITCZ, is broadly consistent
748   with indicators of wind-driven upwelling in the Pacific Antarctic zone.

6 Conclusions

Here we present a new gas-phase ice core climate proxy, Kr-86 excess, that reflects time-averaged surface pressure variability at the site driven by synoptic activity. Surface pressure variability weakly disturbs the gravitational settling and enrichment of the noble gas isotope ratios $\delta^{86}Kr$ and $\delta^{40}Ar$ via barometric pumping. Owing to its higher diffusion coefficient, argon is less affected by this process than krypton is, and therefore the difference $\delta^{86}Kr$-$\delta^{40}Ar$ is a measure of synoptic activity.

This interpretation is supported by a calibration study in which we measure $^{86}Kr_{xs}$ in late Holocene ice core samples from eleven Antarctic and one Greenland ice core that represent a wide range of synoptic activity in the modern climate. Two of the Antarctic cores were rejected due to clear evidence of refrozen melt water. We find a strong correlation ($r = -0.94$ when using site mean data and $r = -0.83$ when using individual samples, $p < 0.01$) between ice core $^{86}Kr_{xs}$ and barometric variability at the site, ~~demonstrating the validity of the new proxy.~~.

Current limitations of the new $^{86}Kr_{xs}$ proxy are: (1) it requires relatively large and non-trivial corrections for gas loss and thermal fractionation; (2) it is moderately sensitive to changes in convective zone thickness; (3) firn air transport models cannot simulate the magnitude of $^{86}Kr_{xs}$ anomalies measured in ice samples; (4) firn air samples show smaller $^{86}Kr_{xs}$ anomalies than ice samples from the same site do; (5) it may be sensitive to the degree of density layering at the site, as a comparison of the nearby Law Dome DE08 and DSSW20K cores suggests; (6) it does not work for warm sites that experience frequent melt; (7) the measurement is challenging (with offsets observed between measurement campaigns), time consuming, and needs large ice samples; and (8) long-term sample storage may impose data offsets. Due to these limitations, we caution that any interpretation of temporal $^{86}Kr_{xs}$ changes remains speculative at present.

Using atmospheric reanalysis data, we show that synoptic-scale barometric variability in Antarctica is primarily linked to the position and/or strength of the southern edge of the eddy-driven subpolar jet (SPJ, also called polar front jet) with a southward SPJ displacement enhancing synoptic-scale surface pressure variability in Antarctica. The commonly-defined modes of large-scale atmospheric variability, such as the southern annular mode and the Pacific-South American pattern, impact Antarctic only weakly as they are weighted towards the mid-latitudes; the exception is the Antarctic Peninsula, where synoptic activity is well-correlated with the southern annular mode ($r = 0.68$). Sites in the Amundsen and Ross Sea sectors are weakly linked to tropical Pacific climate and ENSO ($r = 0.31$ to $r = 0.43$).

We present a new record of $^{86}Kr_{xs}$ from the WAIS Divide ice core in West Antarctica, that covers the last 24ka including the LGM, deglaciation and Holocene. West Antarctic synoptic activity is slightly below modern levels during the last glacial maximum (LGM); increases during the Heinrich Stadial 1 and Younger Dryas North Atlantic cold periods; weakens abruptly at the Holocene onset; remains low during the early and mid-Holocene (up to ~17% below modern), and gradually increases to its modern value. The WDC $^{86}Kr_{xs}$ record resembles records of tropical hydrology and monsoon intensity that are commonly thought to reflect the meridional position of the ITCZ; the sense of the correlation is that WDC synoptic activity is weak when the ITCZ is in its northward position, and vice versa. We interpret the record to reflect migrations of the eddy-driven SPJ in parallel with those of the ITCZ (Ceppi et al., 2013). Secondary influences may come from tropical Pacific climate and ENSO activity. Our $^{86}Kr_{xs}$ record is consistent with weakened ENSO activity (or a more La Niña-like mean state) during the mid- and early Holocene, and

789 enhanced ENSO activity during NH stadial periods – both these features have been described in the paleo-
790 ENSO literature. The inferred changes to the SPJ are broadly consistent with proxies that indicate enhanced
791 wind-driven upwelling in the Pacific Antarctic zone during NH cold stadial periods.

792 Kr-86 excess is a new and potentially useful ice core proxy with the ability to enhance our understanding
793 of past atmospheric circulation. More work to better understand this proxy is warranted, and presently the
794 conclusions of this paper should be considered as tentative. In particular, replication of the deglacial Kr-86
795 excess record presented here in nearby cores is needed before these results can be interpreted with
796 confidence. A full list of suggested follow-up studies is given in section 3.3. Despite the many challenges
797 of Kr-86 excess, its further development is worthwhile owing to the dearth of available proxies for
798 reconstructing SH extratropical atmospheric circulation.

 Appendix A: data corrections

 A1 Gas loss correction

801 Gas loss processes artificially enrich the δ^{40}Ar isotopic ratio used to calculate ^{86}Kr$_{xs}$ (Kobashi et al., 2008b;
802 Severinghaus et al., 2009; Severinghaus et al., 2003). Figure A1B shows the relationships between the two
803 most common gas loss proxies $\delta O_2/N_2$ and $\delta Ar/N_2$ for all samples in the calibration dataset; we find a slope
804 close to the 2:1 slope commonly reported in the literature (Bender et al., 1995); the exception is the DE08-
805 OH site where the data fall on a 1:1 slope. Depletion in fugitive gases (such as O_2 and Ar) represents the
806 sum of losses during bubble closure in the firn (Bender, 2002; Huber et al., 2006; Severinghaus and Battle,
807 2006), and those during drilling, handling, storage, and analysis of the samples (Ikeda-Fukazawa et al.,
808 2005). The patterns are inconsistent with storage conditions alone – for example the DF and EDC cores
809 were stored very cold and SP drilled very recently; yet all three have strong $\delta O_2/N_2$ and $\delta Ar/N_2$ depletion.
810 Natural gas loss from the firn, as well as artefactual loss during drilling likely dominate the signal. The
811 DE08-OH samples were dry-drilled and suffered from poor ice quality for the most depleted samples, which
812 may explain the alternate 1:1 slope at the site (Appendix B); note though that a recent work suggests a ~5:1
813 slope for post-coring gas loss (Oyabu et al., 2021). The DE08-OH samples were also analyzed differently
814 from those at other sites, with $\delta O_2/N_2$ and $\delta Ar/N_2$ measurements performed on a separate smaller ice piece
815 (see section 2.2); the greater surface-to-volume ratio of such small samples may result in greater gas
816 fractionation while evacuating the sample flasks in the laboratory.

817 Severinghaus et al. (2009) hypothesize that the apparent 2:1 slope of $\delta O_2/N_2$ to $\delta Ar/N_2$ depletion is a
818 combination of two mechanisms: size-dependent fractionation during diffusion through the ice lattice, and
819 mass-dependent fractionation (such as molecular or Knudsen diffusion) within ice fractures. In this
820 interpretation, the exact slope would depend on the relative contribution of each process to the total gas
821 loss. It is improbable that both processes would occur in the same ratio at such a wide variety of sites; the
822 2:1 slope is thus more likely an attribute of the gas diffusion rate of gases through ice itself, which is strongly
823 size-dependent, and weakly mass-dependent (Battle et al., 2011).

824 Gas loss is well known to enrich ice samples in δ^{18}O-O_2, and following Severinghaus et al. (2009) we plot
825 δ^{18}O (corrected for gravity and small atmospheric $\delta^{18}O_{atm}$ variations) against gravitationally-corrected
826 $\delta O_2/N_2$ in Fig. A1C. We find a slope of 3.5 per meg enrichment in δ^{18}O per ‰ of $\delta O_2/N_2$ gas loss. This is
827 less than values reported elsewhere (Severinghaus et al., 2009), but provides further evidence for mass-
828 dependent fractionation during gas loss. Our core top dataset further suggests a correlation between
829 δ^{40}Ar - $4\times\delta^{15}$N (a measure of δ^{40}Ar enrichment impacted by both thermal fractionation and gas loss) and
830 gravitationally corrected $\delta Ar/N_2$ (Fig. A1D), suggesting Ar loss leads to enrichment of the remaining δ^{40}Ar.

831 Following Severinghaus et al. (2009), we assume that the δ^{40}Ar correction scales with gas loss indicator
832 $(\delta O_2/N_2 - \delta Ar/N_2)$:

833
$$\Delta_{GL}^{40} = \varepsilon_{40} \times (\delta O_2/N_2 - \delta Ar/N_2)|_{gravcorr} \qquad (A1)$$

834 with Δ_{GL}^{40} the isotopic gas loss correction on δ^{40}Ar and ε_{40} a scaling parameter. Note that gravitationally
835 corrected $\delta O_2/N_2$ and $\delta Ar/N_2$ data are used. Here we rely on data from the Antarctic Byrd ice core for a best

836   estimate of ε_{40} (Fig. A2); some samples from this core suffered extreme gas loss with ($\delta O_2/N_2$ - $\delta Ar/N_2$) as
837   low as -100‰. This data set suggest ε_{40} = -0.008, or 8 per meg $\delta^{40}Ar$ enrichment per ‰ of ($\delta O_2/N_2$ - $\delta Ar/N_2$)
838   gas loss. Because of the 2:1 slope between $\delta O_2/N_2$ and $\delta Ar/N_2$, we find that ($\delta O_2/N_2$ - $\delta Ar/N_2$) $\approx \delta Ar/N_2$
839   and therefore the coefficient ε_{40} would have a similar slope when regressed against $\delta Ar/N_2$ instead of
840   ($\delta O_2/N_2$ - $\delta Ar/N_2$).

841   The value of ε_{40} = -0.008 agrees reasonably well with other studies. Kobashi et al. (2008) compare replicate
842   sample pairs to back out gas loss, and find (statistically significant) correlations between $\delta^{40}Ar$ enrichment
843   and $\delta Ar/N_2$ (again, which is similar to $\delta O_2/N_2$ - $\delta Ar/N_2$). Kobashi et al. (2008) find ε_{40} values of -0.006, -
844   0.005 and +0.007, depending on the depth range and analytical campaign evaluated. The positive value is
845   surprising, given that most observations, as well as theory, suggest ε_{40} should be negative – we consider
846   this a spurious result given the weak $\delta^{40}Ar$ - $\delta Ar/N_2$ correlation in that particular data set. The other two
847   values of ε_{40} are in reasonable agreement with the Byrd value. For the Siple Dome ice core (Severinghaus
848   et al., 2003), regressing $\delta^{40}Ar$ against $\delta Kr/Ar$ gives a slope of +0.007; this implies ε_{40} = -0.007 in good
849   agreement with our findings. Last, our coretop data suggest $\delta^{40}Ar$ enrichment with an ε_{40} value of -0.0072
850   (Fig. A1D), also in good agreement with Byrd.

851   Given the uncertainty in the gas loss parameter, we verify that our results are valid for a wide range of ε_{40}
852   values (Fig. 3B).

853   The downcore WDC $^{86}Kr_{xs}$ was measured over five separate measurement campaigns, with $\delta O_2/N_2$ and
854     $\delta Ar/N_2$ data available only for the first three campaigns.

855   In order to provide a consistent gas loss correction to the five measurement campaigns, including campaigns
856   4 and 5 for which no $\delta O_2/N_2$ or $\delta Ar/N_2$ data are available, we fit a third-order polynomial to all available
857   gravitationally-corrected WDC $\delta O_2/N_2$ - $\delta Ar/N_2$ data (Fig. A5A). We can then calculate the expected WDC
858     $\delta O_2/N_2$ - $\delta Ar/N_2$ at any given age, also in the absence of $\delta O_2/N_2$ and $\delta Ar/N_2$ data. For consistency, we use
859   this correction method for all data seen in Fig. 6. Note that the WDC $\delta O_2/N_2$ - $\delta Ar/N_2$ values are small for
860   all ages, and that therefore the gas loss correction is small for this site.

861   **A2 Thermal correction**

862   In the presence of a temperature gradient, thermal diffusion causes isotopic enrichment towards the colder
863   location. The thermal diffusion sensitivity Ω in units of ‰K^{-1} for the various gases is given as (Grachev
864   and Severinghaus, 2003a, b; Kawamura et al., 2013):

865 $$\Omega^{15} = \frac{8.656}{T} - \frac{1232}{T^2}$$

866 $$\Omega^{40} = \frac{26.08}{T} - \frac{3952}{T^2}$$

867 $$\Omega^{86} = \frac{5.05}{T} - \frac{580}{T^2}$$

868 We estimate the thermal gradient ΔT in the firn using N-15 excess (Severinghaus et al., 1998):

869
$$\Delta T = \frac{^{15}N_{xs}}{\Omega^{15} - \Omega^{40}/4} = \frac{\delta^{15}N - (\delta^{40}Ar + \Delta_{GL}^{40})/4}{\Omega^{15} - \Omega^{40}/4} \tag{A2}$$

870 with Δ_{GL}^{40} the $\delta^{40}Ar$ gas loss correction from Eq. (A1). Positive values of ΔT indicate that the surface is
871 warmer than the firn-ice transition. The ΔT then in turn allows us to estimate the thermal corrections:

872
$$\Delta_{TF}^{15} = -\Omega^{15}\Delta T$$

873
$$\Delta_{TF}^{40} = -\Omega^{40}\Delta T$$

874
$$\Delta_{TF}^{86} = -\Omega^{86}\Delta T \tag{A3}$$

875 The samples from the calibration dataset are from the climatically stable late Holocene period, and typically
876 close together in depth; the uncertainty in the ΔT estimation for individual samples therefore exceeds the
877 temporal variability in ΔT. To reduce the uncertainty in the thermal correction we estimate ΔT for individual
878 samples using Eq. (A2), and for each site average the available data to get a site-average firn temperature
879 gradient $\overline{\Delta T}$. The thermal correction is then given by:

880
$$\Delta_{TF}^{15} = -\Omega^{15}\overline{\Delta T}$$

881
$$\Delta_{TF}^{40} = -\Omega^{40}\overline{\Delta T}$$

882
$$\Delta_{TF}^{86} = -\Omega^{86}\overline{\Delta T} \tag{A4}$$

883 The two methods are compared in Figs. A3C (individual sample ΔT) and A3D (site mean $\overline{\Delta T}$); it is clear
884 that the $\overline{\Delta T}$ approach reduces the spread in $^{86}Kr_{xs}$ (error bars), but not its mean (white dots). The ΔT estimates
885 in individual samples are subject to errors in the isotopic measurements; some of these errors will cancel
886 out in the $\overline{\Delta T}$.

887 For the downcore WDC record through the deglaciation we can no longer assume a stationary ΔT; we
888 instead rely on dynamic firn densification model simulations of ΔT (Buizert et al., 2015). A comparison of
889 the simulated and data-based ΔT is shown in Fig. A5 for WDC. The data clearly show a lot more
890 scatter/variability than the simulations do. We interpret this mainly as analytical noise in the $\delta^{15}N$ and $\delta^{40}Ar$
891 measurements, however, the gas loss correction (Appendix A1) also impacts the ΔT estimation in individual
892 samples. The comparison suggests that the scatter in the ΔT estimates actually exceeds the magnitude of
893 the simulated thermal signals. Using ΔT of the individual samples would thus introduce much scatter in the
894 (thermally corrected) $^{86}Kr_{xs}$ records, and we choose to use the modelled ΔT instead.

895 **A3 Elevation correction**

896 To correct the deglacial WAIS Divide record for elevation changes, we here estimate the $^{86}Kr_{xs}$ dependence
897 on site elevation using the calibration dataset. Note that elevation and synoptic activity are strongly
898 correlated for the investigated sites (r = - 0.86), with synoptic activity decreasing with elevation because
899 the cyclonic systems do not penetrate deeply into the Antarctic interior. Figure A6 shows the result of this
900 exercise. We find a slope of 34 per meg ‰$^{-1}$ of $^{86}Kr_{xs}$ per 1000 m of elevation change, with a correlation of
901 r = 0.96 when considering site-mean $^{86}Kr_{xs}$, and r = 0.86 when considering individual samples. Note that
902 the GISP2 site is not included in the analysis because it is in Greenland where the elevation-$^{86}Kr_{xs}$
903 relationship may be different from Antarctica – it does however fit the Antarctic trend rather well. We
904 further use the simulated WAIS Divide elevation history (Golledge et al., 2014), which simulates an LGM
905 elevation of around 300 m higher than at present at WAIS Divide.

Appendix B: Sub-annual $^{86}Kr_{xs}$ variations at DE08-OH

The Law Dome DE08-OH site is a revisit of the DE08 site, drilled in the 2018/2019 Austral summer Antarctic field season. We have samples from two separate cores: (1) thirteen 24-cm-long samples from a 10-cm-diameter core going from 97 m to 193 m depth at ~ 8 m sample spacing; and (2) eight 6-cm-long samples from a 24-cm-diameter core going from 97.6 m to 99.8 m depth at 30 cm sample spacing. The purpose of the first set was to determine possible long-term variations in $^{86}Kr_{xs}$; the purpose of the second set to assess whether there are sub-annual variations in $^{86}Kr_{xs}$ due to the seasonality in firn properties and bubble trapping.

Both cores were dry-drilled (i.e., no drill liquid was used). The 10-cm-diameter core used was drilled at the beginning of the field season, the 24-cm-diameter core at the end of the field season. Prior to shipment off the continent, both cores were stored in a chest freezer at Casey Station; due to a miscommunication this freezer was set to -20°C rather than -26°C, yet the ice is believed to have stayed below -18°C.

Both DE08-OH cores experienced more gas loss than the original DE08 core that we also sampled (Fig. A1 B). In particular the samples from the 10-cm-diameter core were strongly depleted in $\delta Ar/N_2$, with the most extreme gas loss seen for the deepest samples where the ice quality was poorest.

Fig. B1 shows the high-resolution sub-annual DE08-OH sampling. The data were corrected for gas loss and thermal fractionation, using a site-mean temperature gradient of $\overline{\Delta T}$ = -1.6°C, possibly related to a rectifier effect (Morgan et al. 2022). We find strong (5-fold) variations in $^{86}Kr_{xs}$ on sub-annual time scales. With an expected annual layer thickness of around 1.3 m at this depth, it appears as though there may be an annual-scale variation in $^{86}Kr_{xs}$; the data set has insufficient length to establish this firmly.

We refrain from interpreting the long-term variations in $^{86}Kr_{xs}$ in the 10-cm-diameter core for two reasons. First, given the strong sub-annual variations seen in the high-resolution sampling, it is unavoidable that we are aliasing the underlying signal in the core. Second, the 10-cm-diameter core suffers from strong gas loss (depleted $\delta Ar/N_2$). We attribute this primarily to the dry drilling and imperfect sample storage conditions. Perhaps the greater stresses during drilling a 10-cm core (compared to the 24-cm diameter core) result in more micro-fractures and gas loss.

Supplement

A data supplement is available with this paper.

Data availability

Data are available here: https://www.usap-dc.org/view/project/p0010037, and via the data supplement to this paper.

Author contributions

CB, JS, AJS and EJB designed research; SS, AS, BB, KK, DB, AJS, JDM and IO contributed measurements; KK, DME, NB, RLP, RB, EM-T, PDN, DT, and VVP contributed ice core samples; CB and WHGR analyzed reanalysis data; CB, AJS, and BB performed firn modelling; CB drafted the manuscript with input from all authors.

Competing Interests

The authors declare no competing interests.

Acknowledgements

The idea for the Kr-86 excess proxy came out of discussions at the 2014 WAIS Divide Ice Core Science Meeting held at Scripps Institution of Oceanography in La Jolla, CA. The authors want to thank John Chiang, Justin Wettstein, Zanna Chase, Bob Anderson, Tyler Jones and Eric Steig for useful discussions, data sharing and manuscript feedback, the NSF ice core facility (NSF-ICF, formerly the National Ice Core Laboratory) for curating and distributing ice core samples, the European Centre for Medium-Range Weather Forecasts (ECMWF) for making ERA-Interim reanalysis datasets publicly available, and the US ice drilling program for coordinating ice core drilling in Antarctica. Ice drilling and field support at Law Dome and sample handling in Hobart was provided by the Australian Antarctic Science Program, the Australian Antarctic Division and (at DE08-OH) the U.S. National Science Foundation.

Financial Support

We gratefully acknowledge financial support from the U.S. National Science Foundation (grant numbers ANT-0944343, ANT-1543267, ANT-1543229, ANT-1643716 and ANT-1643669), the New Zealand Ministry of Business, Innovation and Employment (grant numbers RDF-VUW-1103, 15-VUW-131, 540GCT32).

References

959

960 Anderson, R.F., Ali, S., Bradtmiller, L.I., Nielsen, S.H.H., Fleisher, M.Q., Anderson, B.E. and Burckle, L.H. (2009)
961   Wind-Driven Upwelling in the Southern Ocean and the Deglacial Rise in Atmospheric CO2. Science 323, 1443-
962   1448.
963 Baggenstos, D., Häberli, M., Schmitt, J., Shackleton, S.A., Birner, B., Severinghaus, J.P., Kellerhals, T. and Fischer,
964   H. (2019) Earth's radiative imbalance from the Last Glacial Maximum to the present. Proc. Natl. Acad. Sci. U. S.
965   A., 201905447.
966 Bals-Elsholz, T.M., Atallah, E.H., Bosart, L.F., Wasula, T.A., Cempa, M.J. and Lupo, A.R. (2001) The Wintertime
967   Southern Hemisphere Split Jet: Structure, Variability, and Evolution. J. Clim. 14, 4191-4215.
968 Battle, M.O., Severinghaus, J.P., Sofen, E.D., Plotkin, D., Orsi, A.J., Aydin, M., Montzka, S.A., Sowers, T. and Tans,
969   P.P. (2011) Controls on the movement and composition of firn air at the West Antarctic Ice Sheet Divide. Atmos.
970   Chem. Phys. 11, 11007-11021.
971 Bender, M., Sowers, T. and Lipenkov, V. (1995) ON THE CONCENTRATIONS OF O-2, N-2, AND AR IN
972   TRAPPED GASES FROM ICE CORES. J. Geophys. Res. 100, 18651-18660.
973 Bender, M.L. (2002) Orbital tuning chronology for the Vostok climate record supported by trapped gas composition.
974   Earth Planet. Sci. Lett. 204, 275-289.
975 Bereiter, B., Kawamura, K. and Severinghaus, J.P. (2018a) New methods for measuring atmospheric heavy noble gas
976   isotope and elemental ratios in ice core samples. Rapid communications in mass spectrometry 32, 801-814.
977 Bereiter, B., Shackleton, S., Baggenstos, D., Kawamura, K. and Severinghaus, J. (2018b) Mean global ocean
978   temperatures during the last glacial transition. Nature 553, 39.
979 Birner, B., Buizert, C., Wagner, T.J.W. and Severinghaus, J.P. (2018) The influence of layering and barometric
980   pumping on firn air transport in a 2-D model. The Cryosphere 12, 2021-2037.
981 Braconnot, P., Luan, Y., Brewer, S. and Zheng, W. (2012) Impact of Earth's orbit and freshwater fluxes on Holocene
982   climate mean seasonal cycle and ENSO characteristics. Clim. Dyn. 38, 1081-1092.
983 Broccoli, A.J., Dahl, K.A. and Stouffer, R.J. (2006) Response of the ITCZ to Northern Hemisphere cooling. Geophys.
984   Res. Lett. 33, L01702.
985 Buizert, C., Cuffey, K.M., Severinghaus, J.P., Baggenstos, D., Fudge, T.J., Steig, E.J., Markle, B.R., Winstrup, M.,
986   Rhodes, R.H., Brook, E.J., Sowers, T.A., Clow, G.D., Cheng, H., Edwards, L.R., Sigl, M., McConnell, J.R. and
987   Taylor, K.C. (2015) The WAIS Divide deep ice core WD2014 chronology - part 1: Methane synchronization (68-
988   31 ka BP) and the gas age-ice age difference. Climate of the Past 11, 153-173.
989 Buizert, C. and Severinghaus, J.P. (2016) Dispersion in deep polar firn driven by synoptic-scale surface pressure
990   variability. The Cryosphere 10, 2099-2111.
991 Buizert, C., Sigl, M., Severi, M., Markle, B.R., Wettstein, J.J., McConnell, J.R., Pedro, J.B., Sodemann, H., Goto-
992   Azuma, K., Kawamura, K., Fujita, S., Motoyama, H., Hirabayashi, M., Uemura, R., Stenni, B., Parrenin, F., He,
993   F., Fudge, T.J. and Steig, E.J. (2018) Abrupt ice-age shifts in southern westerly winds and Antarctic climate forced
994   from the north. Nature 563, 681-685.
995 Buizert, C., Sowers, T. and Blunier, T. (2013) Assessment of diffusive isotopic fractionation in polar firn, and
996   application to ice core trace gas records. Earth Planet. Sci. Lett. 361, 110-119.
997 Cai, W., Santoso, A., Wang, G., Yeh, S.-W., An, S.-I., Cobb, K.M., Collins, M., Guilyardi, E., Jin, F.-F., Kug, J.-S.,
998   Lengaigne, M., McPhaden, M.J., Takahashi, K., Timmermann, A., Vecchi, G., Watanabe, M. and Wu, L. (2015)
999   ENSO and greenhouse warming. Nature Clim. Change 5, 849-859.
1000 Cane, M.A. (2005) The evolution of El Niño, past and future. Earth Planet. Sci. Lett. 230, 227-240.
1001 Ceppi, P., Hwang, Y.-T., Liu, X., Frierson, D.M.W. and Hartmann, D.L. (2013) The relationship between the ITCZ
1002   and the Southern Hemispheric eddy-driven jet. J. Geophys. Res. 118, 5136-5146.
1003 Chase, Z., Anderson, R.F., Fleisher, M.Q. and Kubik, P.W. (2003) Accumulation of biogenic and lithogenic material
1004   in the Pacific sector of the Southern Ocean during the past 40,000 years. Deep Sea Research Part II: Topical Studies
1005   in Oceanography 50, 799-832.
1006 Cheng, H., Edwards, R.L., Sinha, A., Spötl, C., Yi, L., Chen, S., Kelly, M., Kathayat, G., Wang, X., Li, X., Kong, X.,
1007   Wang, Y., Ning, Y. and Zhang, H. (2016) The Asian monsoon over the past 640,000 years and ice age terminations.
1008   Nature 534, 640-646.
1009 Chiang, J.C. and Friedman, A.R. (2012) Extratropical cooling, interhemispheric thermal gradients, and tropical
1010   climate change. Annu. Rev. Earth Planet. Sci. 40, 383-412.
1011 Chiang, J.C.H. and Bitz, C.M. (2005) Influence of high latitude ice cover on the marine Intertropical Convergence
1012   Zone. Clim. Dyn. 25, 477-496.

1013 Chiang, J.C.H., Lee, S.-Y., Putnam, A.E. and Wang, X. (2014) South Pacific Split Jet, ITCZ shifts, and atmospheric
1014 North–South linkages during abrupt climate changes of the last glacial period. Earth Planet. Sci. Lett. 406, 233-
1015 246.
1016 Clement, A.C., Seager, R. and Cane, M.A. (2000) Suppression of El Niño during the Mid-Holocene by changes in the
1017 Earth's orbit. Paleoceanography 15, 731-737.
1018 Cobb, K.M., Westphal, N., Sayani, H.R., Watson, J.T., Di Lorenzo, E., Cheng, H., Edwards, R.L. and Charles, C.D.
1019 (2013) Highly Variable El Niño–Southern Oscillation Throughout the Holocene. Science 339, 67-70.
1020 Conroy, J.L., Overpeck, J.T., Cole, J.E., Shanahan, T.M. and Steinitz-Kannan, M. (2008) Holocene changes in eastern
1021 tropical Pacific climate inferred from a Galápagos lake sediment record. Quat. Sci. Rev. 27, 1166-1180.
1022 Cruz, F.W., Burns, S.J., Karmann, I., Sharp, W.D., Vuille, M., Cardoso, A.O., Ferrari, J.A., Dias, P.L.S. and Viana,
1023 O. (2005) Insolation-driven changes in atmospheric circulation over the past 116,000 years in subtropical Brazil.
1024 Nature 434, 63-66.
1025 Dee, D.P., Uppala, S.M., Simmons, A.J., Berrisford, P., Poli, P., Kobayashi, S., Andrae, U., Balmaseda, M.A.,
1026 Balsamo, G., Bauer, P., Bechtold, P., Beljaars, A.C.M., van de Berg, L., Bidlot, J., Bormann, N., Delsol, C.,
1027 Dragani, R., Fuentes, M., Geer, A.J., Haimberger, L., Healy, S.B., Hersbach, H., Hólm, E.V., Isaksen, L., Kållberg,
1028 P., Köhler, M., Matricardi, M., McNally, A.P., Monge-Sanz, B.M., Morcrette, J.J., Park, B.K., Peubey, C., de
1029 Rosnay, P., Tavolato, C., Thépaut, J.N. and Vitart, F. (2011) The ERA-Interim reanalysis: configuration and
1030 performance of the data assimilation system. Quarterly Journal of the Royal Meteorological Society 137, 553-597.
1031 Driscoll, R., Elliot, M., Russon, T., Welsh, K., Yokoyama, Y. and Tudhope, A. (2014) ENSO reconstructions over the
1032 past 60 ka using giant clams (Tridacna sp.) from Papua New Guinea. Geophys. Res. Lett. 41, 6819-6825.
1033 Dykoski, C.A., Edwards, R.L., Cheng, H., Yuan, D.X., Cai, Y.J., Zhang, M.L., Lin, Y.S., Qing, J.M., An, Z.S. and
1034 Revenaugh, J. (2005) A high-resolution, absolute-dated Holocene and deglacial Asian monsoon record from
1035 Dongge Cave, China. Earth Planet. Sci. Lett. 233, 71-86.
1036 Emile-Geay, J., Cobb, K.M., Carré, M., Braconnot, P., Leloup, J., Zhou, Y., Harrison, S.P., Corrège, T., McGregor,
1037 H.V., Collins, M., Driscoll, R., Elliot, M., Schneider, B. and Tudhope, A. (2015) Links between tropical Pacific
1038 seasonal, interannual and orbital variability during the Holocene. Nat. Geosci. 9, 168.
1039 Etheridge, D.M., Pearman, G.I. and Fraser, P.J. (1992) CHANGES IN TROPOSPHERIC METHANE BETWEEN
1040 1841 AND 1978 FROM A HIGH ACCUMULATION-RATE ANTARCTIC ICE CORE. Tellus 44, 282-294.
1041 Fahnestock, M.A., Scambos, T.A., Shuman, C.A., Arthern, R.J., Winebrenner, D.P. and Kwok, R. (2000) Snow
1042 megadune fields on the East Antarctic Plateau: Extreme atmosphere-ice interaction. Geophys. Res. Lett. 27, 3719-
1043 3722.
1044 Fowler, A.M., Boswijk, G., Lorrey, A.M., Gergis, J., Pirie, M., McCloskey, S.P.J., Palmer, J.G. and Wunder, J. (2012)
1045 Multi-centennial tree-ring record of ENSO-related activity in New Zealand. Nature Climate Change 2, 172.
1046 Fujita, S., Okuyama, J., Hori, A. and Hondoh, T. (2009) Metamorphism of stratified firn at Dome Fuji, Antarctica: A
1047 mechanism for local insolation modulation of gas transport conditions during bubble close off. J. Geophys. Res.
1048 114.
1049 Gergis, J.L. and Fowler, A.M. (2009) A history of ENSO events since A.D. 1525: implications for future climate
1050 change. Clim. Change 92, 343-387.
1051 Golledge, N.R., Menviel, L., Carter, L., Fogwill, C.J., England, M.H., Cortese, G. and Levy, R.H. (2014) Antarctic
1052 contribution to meltwater pulse 1A from reduced Southern Ocean overturning. Nat Comm. 5, 5107.
1053 Grachev, A.M. and Severinghaus, J.P. (2003a) Determining the thermal diffusion factor for Ar-40/Ar-36 in air to aid
1054 paleoreconstruction of abrupt climate change. J. Phys. Chem. A 107, 4636-4642.
1055 Grachev, A.M. and Severinghaus, J.P. (2003b) Laboratory determination of thermal diffusion constants for N-
1056 29(2)/N-28(2) in air at temperatures from-60 to 0 degrees C for reconstruction of magnitudes of abrupt climate
1057 changes using the ice core fossil-air paleothermometer. Geochim. Cosmochim. Acta 67, 345-360.
1058 Grootes, P.M., Stuiver, M., White, J.W.C., Johnsen, S. and Jouzel, J. (1993) Comparison of oxygen isotope records
1059 from the GISP2 and GRIP Greenland ice cores. Nature 366, 552-554.
1060 Headly, M.A. and Severinghaus, J.P. (2007) A method to measure Kr/N-2 ratios in air bubbles trapped in ice cores
1061 and its application in reconstructing past mean ocean temperature. J. Geophys. Res. 112, 12.
1062 Herron, M.M. and Langway, C.C. (1980) Firn densification: An empirical model. J. Glaciol. 25, 373-385.
1063 Huang, B., Banzon, V.F., Freeman, E., Lawrimore, J., Liu, W., Peterson, T.C., Smith, T.M., Thorne, P.W., Woodruff,
1064 S.D. and Zhang, H.-M. (2014) Extended Reconstructed Sea Surface Temperature Version 4 (ERSST.v4). Part I:
1065 Upgrades and Intercomparisons. J. Clim. 28, 911-930.
1066 Huber, C., Beyerle, U., Leuenberger, M., Schwander, J., Kipfer, R., Spahni, R., Severinghaus, J.P. and Weiler, K.
1067 (2006) Evidence for molecular size dependent gas fractionation in firn air derived from noble gases, oxygen, and
1068 nitrogen measurements. Earth Planet. Sci. Lett. 243, 61-73.

1069   Ikeda-Fukazawa, T., Fukumizu, K., Kawamura, K., Aoki, S., Nakazawa, T. and Hondoh, T. (2005) Effects of
1070   molecular diffusion on trapped gas composition in polar ice cores. Earth Planet. Sci. Lett. 229, 183-192.
1071   Kanner, L.C., Burns, S.J., Cheng, H. and Edwards, R.L. (2012) High-Latitude Forcing of the South American Summer
1072   Monsoon During the Last Glacial. Science 335, 570-573
1073   Kawamura, K., Severinghaus, J.P., Albert, M.R., Courville, Z.R., Fahnestock, M.A., Scambos, T., Shields, E. and
1074   Shuman, C.A. (2013) Kinetic fractionation of gases by deep air convection in polar firn. Atmos. Chem. Phys. 13,
1075   11141-11155.
1076   Kawamura, K., Severinghaus, J.P., Ishidoya, S., Sugawara, S., Hashida, G., Motoyama, H., Fujii, Y., Aoki, S. and
1077   Nakazawa, T. (2006) Convective mixing of air in firn at four polar sites. Earth Planet. Sci. Lett. 244, 672-682.
1078   Kobashi, T., Severinghaus, J.P. and Barnola, J.M. (2008a) 4 +/- 1.5 degrees C abrupt warming 11,270 yr ago identified
1079   from trapped air in Greenland ice. Earth Planet. Sci. Lett. 268, 397-407.
1080   Kobashi, T., Severinghaus, J.P. and Kawamura, K. (2008b) Argon and nitrogen isotopes of trapped air in the GISP2
1081   ice core during the Holocene epoch (0-11,500 B.P.): Methodology and implications for gas loss processes.
1082   Geochim. Cosmochim. Acta 72, 4675-4686.
1083   Kohfeld, K.E., Graham, R.M., de Boer, A.M., Sime, L.C., Wolff, E.W., Le Quéré, C. and Bopp, L. (2013) Southern
1084   Hemisphere westerly wind changes during the Last Glacial Maximum: paleo-data synthesis. Quat. Sci. Rev. 68,
1085   76-95.
1086   Koutavas, A., deMenocal, P.B., Olive, G.C. and Lynch-Stieglitz, J. (2006) Mid-Holocene El Niño–Southern
1087   Oscillation (ENSO) attenuation revealed by individual foraminifera in eastern tropical Pacific sediments. Geology
1088   34, 993-996.
1089   Koutavas, A., Lynch-Stieglitz, J., Marchitto, T.M. and Sachs, J.P. (2002) El Niño-Like Pattern in Ice Age Tropical
1090   Pacific Sea Surface Temperature. Science 297, 226-230.
1091   Lamy, F., Chiang, J.C.H., Martínez-Méndez, G., Thierens, M., Arz, H.W., Bosmans, J., Hebbeln, D., Lambert, F.,
1092   Lembke-Jene, L. and Stuut, J.-B. (2019) Precession modulation of the South Pacific westerly wind belt over the
1093   past million years. Proc. Natl. Acad. Sci. U. S. A., 201905847.
1094   Lee, S. and Kim, H.-k. (2003) The Dynamical Relationship between Subtropical and Eddy-Driven Jets. Journal of the
1095   Atmospheric Sciences 60, 1490-1503.
1096   Lee, S.Y., Chiang, J.C., Matsumoto, K. and Tokos, K.S. (2011) Southern Ocean wind response to North Atlantic
1097   cooling and the rise in atmospheric CO2: Modeling perspective and paleoceanographic implications.
1098   Paleoceanography 26.
1099   Liu, Z., Kutzbach, J. and Wu, L. (2000) Modeling climate shift of El Nino variability in the Holocene. Geophys. Res.
1100   Lett. 27, 2265-2268.
1101   Liu, Z., Lu, Z., Wen, X., Otto-Bliesner, B.L., Timmermann, A. and Cobb, K.M. (2014) Evolution and forcing
1102   mechanisms of El Nino over the past 21,000 years. Nature 515, 550-553.
1103   Lynch-Stieglitz, J. (2017) The Atlantic Meridional Overturning Circulation and Abrupt Climate Change. Annual
1104   Review of Marine Science 9, 83-104.
1105   Mantua, N.J. and Hare, S.R. (2002) The Pacific Decadal Oscillation. Journal of Oceanography 58, 35-44.
1106   Marcott, S.A., Shakun, J.D., Clark, P.U. and Mix, A.C. (2013) A Reconstruction of Regional and Global Temperature
1107   for the Past 11,300 Years. Science 339, 1198-1201.
1108   Marino, G., Zahn, R., Ziegler, M., Purcell, C., Knorr, G., Hall, I.R., Ziveri, P. and Elderfield, H. (2013) Agulhas salt-
1109   leakage oscillations during abrupt climate changes of the Late Pleistocene. Paleoceanography 28, 599-606.
1110   Markle, B.R., Steig, E.J., Buizert, C., Schoenemann, S.W., Bitz, C.M., Fudge, T.J., Pedro, J.B., Ding, Q., Jones, T.R.,
1111   White, J.W.C. and Sowers, T. (2017) Global atmospheric teleconnections during Dansgaard-Oeschger events.
1112   Nature Geosci 10, 36-40.
1113   Marshall, J. and Speer, K. (2012) Closure of the meridional overturning circulation through Southern Ocean
1114   upwelling. Nature Geosci 5, 171-180.
1115   McGee, D., Donohoe, A., Marshall, J. and Ferreira, D. (2014) Changes in ITCZ location and cross-equatorial heat
1116   transport at the Last Glacial Maximum, Heinrich Stadial 1, and the mid-Holocene. Earth Planet. Sci. Lett. 390, 69-
1117   79.
1118   Merkel, U., Prange, M. and Schulz, M. (2010) ENSO variability and teleconnections during glacial climates. Quat.
1119   Sci. Rev. 29, 86-100.
1120   Mo, K.C. and Paegle, J.N. (2001) The Pacific–South American modes and their downstream effects. International
1121   Journal of Climatology 21, 1211-1229.
1122   Moy, C.M., Seltzer, G.O., Rodbell, D.T. and Anderson, D.M. (2002) Variability of El Niño/Southern Oscillation
1123   activity at millennial timescales during the Holocene epoch. Nature 420, 162.

1124 Nakamura, H. and Shimpo, A. (2004) Seasonal Variations in the Southern Hemisphere Storm Tracks and Jet Streams
1125   as Revealed in a Reanalysis Dataset. J. Clim. 17, 1828-1844.
1126 Orsi, A.J., Kawamura, K., Fegyveresi, J.M., Headly, M.A., Alley, R.B. and Severinghaus, J.P. (2015) Differentiating
1127   bubble-free layers from melt layers in ice cores using noble gases. J. Glaciol. 61, 585-594.
1128 Oyabu, I., Kawamura, K., Uchida, T., Fujita, S., Kitamura, K., Hirabayashi, M., Aoki, S., Morimoto, S., Nakazawa,
1129   T., Severinghaus, J.P. and Morgan, J.D. (2021) Fractionation of O2∕N2 and Ar∕N2 in the Antarctic ice sheet during
1130   bubble formation and bubble–clathrate hydrate transition from precise gas measurements of the Dome Fuji ice
1131   core. The Cryosphere 15, 5529-5555.
1132 Parkinson, C.L. and Cavalieri, D.J. (2012) Antarctic sea ice variability and trends, 1979–2010. The Cryosphere
1133   6, 871-880.
1134 Pedro, J.B., Jochum, M., Buizert, C., He, F., Barker, S. and Rasmussen, S.O. (2018) Beyond the bipolar seesaw:
1135   Toward a process understanding of interhemispheric coupling. Quat. Sci. Rev. 192, 27-46.
1136 Peterson, L.C., Haug, G.H., Hughen, K.A. and Röhl, U. (2000) Rapid Changes in the Hydrologic Cycle of the Tropical
1137   Atlantic During the Last Glacial. Science 290, 1947-1951.
1138 Rahmstorf, S. (2002) Ocean circulation and climate during the past 120,000 years. Nature 419, 207-214.
1139 Raynaud, D., Lipenkov, V., Lemieux-Dudon, B., Duval, P., Loutre, M.F. and Lhomme, N. (2007) The local insolation
1140   signature of air content in Antarctic ice. A new step toward an absolute dating of ice records. Earth Planet. Sci.
1141   Lett. 261, 337-349.
1142 Rein, B., Lückge, A., Reinhardt, L., Sirocko, F., Wolf, A. and Dullo, W.-C. (2005) El Niño variability off Peru during
1143   the last 20,000 years. Paleoceanography 20.
1144 Rhodes, R.H., Faïn, X., Brook, E.J., McConnell, J.R., Maselli, O.J., Sigl, M., Edwards, J., Buizert, C., Blunier, T.,
1145   Chappellaz, J. and Freitag, J. (2016) Local artifacts in ice core methane records caused by layered bubble trapping
1146   and in situ production: a multi-site investigation. Clim. Past 12, 1061-1077.
1147 Riedinger, M.A., Steinitz-Kannan, M., Last, W.M. and Brenner, M. (2002) A ~6100 14C yr record of El Niño activity
1148   from the Galápagos Islands. Journal of Paleolimnology 27, 1-7.
1149 Rind, D., Russell, G., Schmidt, G., Sheth, S., Collins, D., Demenocal, P. and Teller, J. (2001) Effects of glacial
1150   meltwater in the GISS coupled atmosphere-ocean model: 2. A bipolar seesaw in Atlantic Deep Water production.
1151   Journal of Geophysical Research: Atmospheres (1984–2012) 106, 27355-27365.
1152 Rojas, M., Moreno, P., Kageyama, M., Crucifix, M., Hewitt, C., Abe-Ouchi, A., Ohgaito, R., Brady, E.C. and Hope,
1153   P. (2009) The Southern Westerlies during the last glacial maximum in PMIP2 simulations. Clim. Dyn. 32, 525-
1154   548.
1155 Rommelaere, V., Arnaud, L., and Barnola, J.M. (1997) Reconstructing recent atmospheric trace gas concentrations
1156   from polar firn and bubbly ice data by inverse methods. J. Geophys. Res. 102, 30069-30083.
1157 Russell, J.L., Dixon, K.W., Gnanadesikan, A., Stouffer, R.J. and Toggweiler, J.R. (2006) The Southern Hemisphere
1158   Westerlies in a Warming World: Propping Open the Door to the Deep Ocean. J. Clim. 19, 6382-6390.
1159 Sadekov, A.Y., Ganeshram, R., Pichevin, L., Berdin, R., McClymont, E., Elderfield, H. and Tudhope, A.W. (2013)
1160   Palaeoclimate reconstructions reveal a strong link between El Niño-Southern Oscillation and Tropical Pacific mean
1161   state. Nature Communications 4, 2692.
1162 Salau, O., Schneider, B., Park, W., Khon, V. and Latif, M. (2012) Modeling the ENSO impact of orbitally induced
1163   mean state climate changes. J. Geophys. Res. 117.
1164 Schaller, C.F., Freitag, J. and Eisen, O. (2017) Critical porosity of gas enclosure in polar firn independent of climate.
1165   Clim. Past 13, 1685-1693.
1166 Schneider, T., Bischoff, T. and Haug, G.H. (2014) Migrations and dynamics of the intertropical convergence zone.
1167   Nature 513, 45-53.
1168 Schwander, J. (1989) The transformation of snow to ice and the occlusion of gases in: Oescher, H., Langway, C.C.
1169   (Eds.), The Environmental record in glaciers and ice sheets. John Wiley, New York, pp. 53-67.
1170 Schwander, J., Barnola, J.M., Andrie, C., Leuenberger, M., Ludin, A., Raynaud, D. and Stauffer, B. (1993) THE AGE
1171   OF THE AIR IN THE FIRN AND THE ICE AT SUMMIT, GREENLAND. J. Geophys. Res. 98, 2831-2838.
1172 Schwander, J., Stauffer, B. and Sigg, A. (1988) Air mixing in firn and the age of the air at pore close-off, Annals of
1173   Glaciology, pp. 141-145.
1174 Severinghaus, J.P., Albert, M.R., Courville, Z.R., Fahnestock, M.A., Kawamura, K., Montzka, S.A., Muhle, J.,
1175   Scambos, T.A., Shields, E., Shuman, C.A., Suwa, M., Tans, P. and Weiss, R.F. (2010) Deep air convection in the
1176   firn at a zero-accumulation site, central Antarctica. Earth Planet. Sci. Lett. 293, 359-367.
1177 Severinghaus, J.P. and Battle, M.O. (2006) Fractionation of gases in polar ice during bubble close-off: New constraints
1178   from firn air Ne, Kr and Xe observations. Earth Planet. Sci. Lett. 244, 474-500.

1179 Severinghaus, J.P., Beaudette, R., Headly, M.A., Taylor, K. and Brook, E.J. (2009) Oxygen-18 of O2 Records the
1180   Impact of Abrupt Climate Change on the Terrestrial Biosphere. Science 324, 1431-1434.
1181 Severinghaus, J.P., Grachev, A., Luz, B. and Caillon, N. (2003) A method for precise measurement of argon 40/36
1182   and krypton/argon ratios in trapped air in polar ice with applications to past firn thickness and abrupt climate
1183   change in Greenland and at Siple Dome, Antarctica. Geochim. Cosmochim. Acta 67, 325-343.
1184 Severinghaus, J.P., Sowers, T., Brook, E.J., Alley, R.B. and Bender, M.L. (1998) Timing of abrupt climate change at
1185   the end of the Younger Dryas interval from thermally fractionated gases in polar ice. Nature 391, 141-146.
1186 Shakun, J.D., Clark, P.U., He, F., Marcott, S.A., Mix, A.C., Liu, Z., Otto-Bliesner, B., Schmittner, A. and Bard, E.
1187   (2012) Global warming preceded by increasing carbon dioxide concentrations during the last deglaciation. Nature
1188   484, 49-54.
1189 Sime, L.C., Kohfeld, K.E., Le Quéré, C., Wolff, E.W., de Boer, A.M., Graham, R.M. and Bopp, L. (2013) Southern
1190   Hemisphere westerly wind changes during the Last Glacial Maximum: model-data comparison. Quat. Sci. Rev.
1191   64, 104-120.
1192 Simpson, I.R., Hitchcock, P., Shepherd, T.G. and Scinocca, J.F. (2011) Stratospheric variability and tropospheric
1193   annular-mode timescales. Geophys. Res. Lett. 38.
1194 Sowers, T., Bender, M., Raynaud, D. and Korotkevich, Y.S. (1992) $\delta^{15}N$ of N2 in air trapped in polar ice: A tracer
1195   of gas transport in the firn and a possible constraint on ice age-gas age differences. J. Geophys. Res. 97, 15683-
1196   15697.
1197 Stott, L., Poulsen, C., Lund, S. and Thunell, R. (2002) Super ENSO and Global Climate Oscillations at Millennial
1198   Time Scales. Science 297, 222-226.
1199 Studer, A.S., Sigman, D.M., Martínez-García, A., Benz, V., Winckler, G., Kuhn, G., Esper, O., Lamy, F., Jaccard,
1200   S.L., Wacker, L., Oleynik, S., Gersonde, R. and Haug, G.H. (2015) Antarctic Zone nutrient conditions during the
1201   last two glacial cycles. Paleoceanography 30, 2014PA002745.
1202 Studer, A.S., Sigman, D.M., Martínez-García, A., Thöle, L.M., Michel, E., Jaccard, S.L., Lippold, J.A., Mazaud, A.,
1203   Wang, X.T., Robinson, L.F., Adkins, J.F. and Haug, G.H. (2018) Increased nutrient supply to the Southern Ocean
1204   during the Holocene and its implications for the pre-industrial atmospheric CO2 rise. Nat. Geosci. 11, 756-760.
1205 Thomas, E.R., Marshall, G.J. and McConnell, J.R. (2008) A doubling in snow accumulation in the western Antarctic
1206   Peninsula since 1850. Geophys. Res. Lett. 35.
1207 Thompson, D.W.J. and Wallace, J.M. (2000) Annular Modes in the Extratropical Circulation. Part I: Month-to-Month
1208   Variability*. J. Clim. 13, 1000-1016.
1209 Thompson, L.G., Mosley-Thompson, E., Davis, M.E., Zagorodnov, V.S., Howat, I.M., Mikhalenko, V.N. and Lin, P.-
1210   N. (2013) Annually Resolved Ice Core Records of Tropical Climate Variability over the Past ~1800 Years. Science
1211   340, 945-950.
1212 Timmermann, A., Okumura, Y., An, S.I., Clement, A., Dong, B., Guilyardi, E., Hu, A., Jungclaus, J.H., Renold, M.,
1213   Stocker, T.F., Stouffer, R.J., Sutton, R., Xie, S.P. and Yin, J. (2007) The Influence of a Weakening of the Atlantic
1214   Meridional Overturning Circulation on ENSO. J. Clim. 20, 4899-4919.
1215 Toggweiler, J.R., Russell, J.L. and Carson, S.R. (2006) Midlatitude westerlies, atmospheric CO2, and climate change
1216   during the ice ages. Paleoceanography 21, PA2005.
1217 Trenberth, K.E. (1991) Storm Tracks in the Southern Hemisphere. Journal of the Atmospheric Sciences 48, 2159-
1218   2178.
1219 Tudhope, A.W., Chilcott, C.P., McCulloch, M.T., Cook, E.R., Chappell, J., Ellam, R.M., Lea, D.W., Lough, J.M. and
1220   Shimmield, G.B. (2001) Variability in the El Niño-Southern Oscillation through a glacial-interglacial cycle.
1221   Science 291, 1511-1517.
1222 Wang, X., Auler, A.S., Edwards, R.L., Cheng, H., Ito, E., Wang, Y., Kong, X. and Solheid, M. (2007) Millennial-
1223   scale precipitation changes in southern Brazil over the past 90,000 years. Geophys. Res. Lett. 34.
1224 Wang, Y.J., Cheng, H., Edwards, R.L., An, Z.S., Wu, J.Y., Shen, C.C. and Dorale, J.A. (2001) A High-Resolution
1225   Absolute-Dated Late Pleistocene Monsoon Record from Hulu Cave, China. Science 294, 2345-2348.
1226 Zheng, W., Braconnot, P., Guilyardi, E., Merkel, U. and Yu, Y. (2008) ENSO at 6ka and 21ka from ocean–atmosphere
1227   coupled model simulations. Clim. Dyn. 30, 745-762.
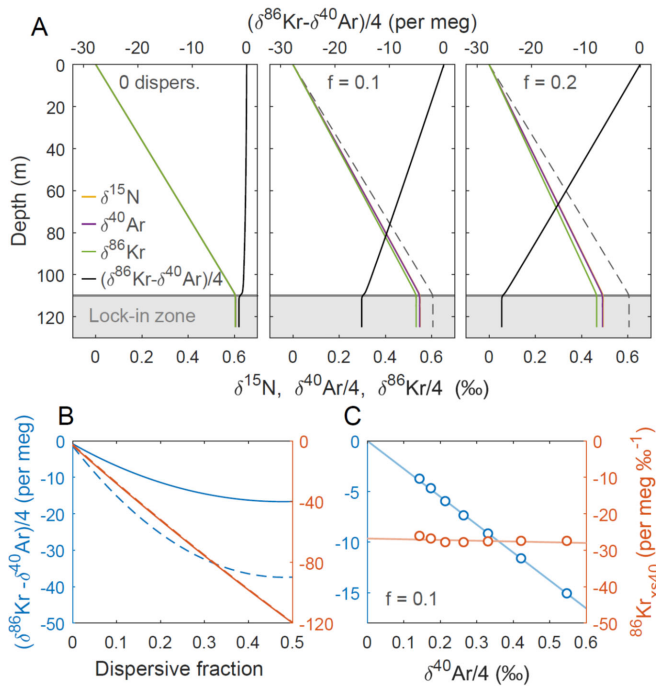
1228

Figure 1. Idealized firn air transport model experiments of $^{86}Kr_{xs}$. Firn density is calculated using (Herron and Langway, 1980), and the diffusivity using (Schwander, 1989). **A** Simulations using a fraction of dispersive mixing of $f = 0$ (left), $f = 0.1$ (middle) and $f = 0.2$ (right) for a hypothetical site with accumulation rate of $A = 2$ cm a^{-1} ice equivalent and mean annual temperature $T = -60°C$. At dispersive fraction f, effective molecular diffusivity of all gases is multiplied by $(1-f)$ and dispersive mixing for all gases is set equal to f times the effective molecular diffusivity of CO_2. **B** Isotopic disequilibrium as a function of dispersive mixing intensity at two different firn thicknesses of around 100 m (dashed, $A = 2$ cm a^{-1} and $T = -60°C$) and 50 m (solid, $A = 2$ cm a^{-1} and $T = -43°C$). We compare isotopic disequilibrium without (blue, left axis) and with (orange, right axis) normalization. **C** Simulations at 10 % dispersive mixing, where each dot represents different climatic conditions. Accumulation rate is $A = 2$ cm a^{-1} ice equivalent and mean annual temperature is changed from -60°C to -30°C in steps of 5°C.
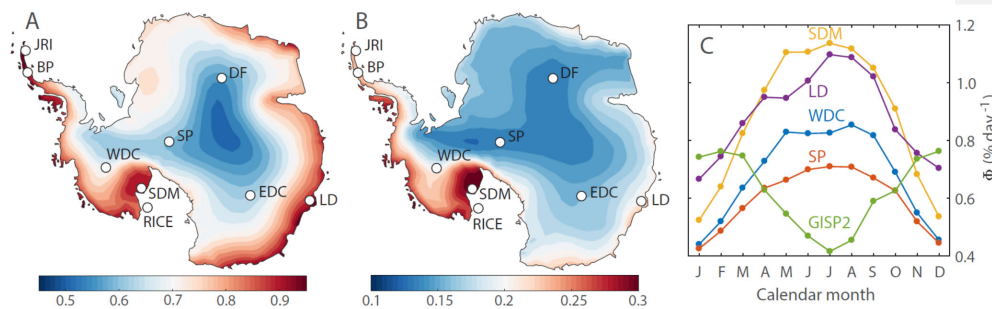
1240

1241

Figure 2. Calibrating Kr-86 excess. **A** Annual-mean Φ in Antarctica over 1979-2017, in units of % day^{-1}. **B** Interannual variability (1σ standard deviation) of annual-mean Φ over 1979-2017, in units of % day^{-1}. **C** Annual cycle in Φ for 1979-2017 for the indicated sites.
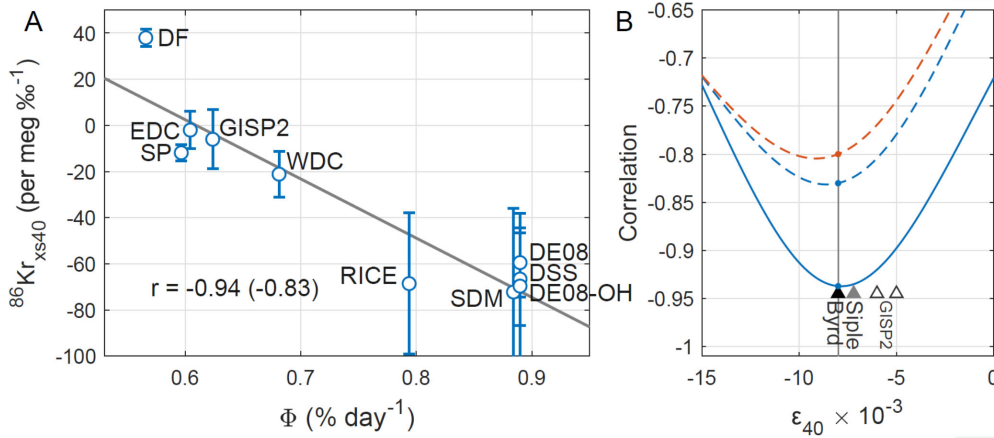
1245

Figure 3. Calibrating Kr-86 excess. **A** $^{86}Kr_{xs}$ as a function of Φ for the calibration data set. Circles give the site mean, and the error bars denote the $\pm 1\sigma$ standard deviation between samples (uncertainty in corrections and measurements not included). The number of samples at each site is given in Table 1. Pearson correlation coefficient is $r = -0.94$ when considering site data means and $r = -0.83$ when considering all individual samples. Data are corrected for gas loss using $\varepsilon_{40} = -0.008$ (Appendix A1), and corrected for thermal fractionation using site-mean ~~N-15~~ ^{15}N excess (Appendix A2). The calibration curve for $^{86}Kr_{xs15}$ is identical in this case, with slightly larger errorbars. **B** Correlation of the calibration curve as a function of the gas loss correction scaling parameter ε_{40}. The solid line gives the correlation for both site-mean $^{86}Kr_{xs15}$ and $^{86}Kr_{xs40}$ (identical); the dashed lines the correlation using individual samples for $^{86}Kr_{xs40}$ (blue) and $^{86}Kr_{xs15}$ (orange). Triangles denote the ε_{40} estimate from the Byrd, Siple and GISP2 ice cores (Fig. A2; Kobashi et al., 2008a; Severinghaus et al., 2003).
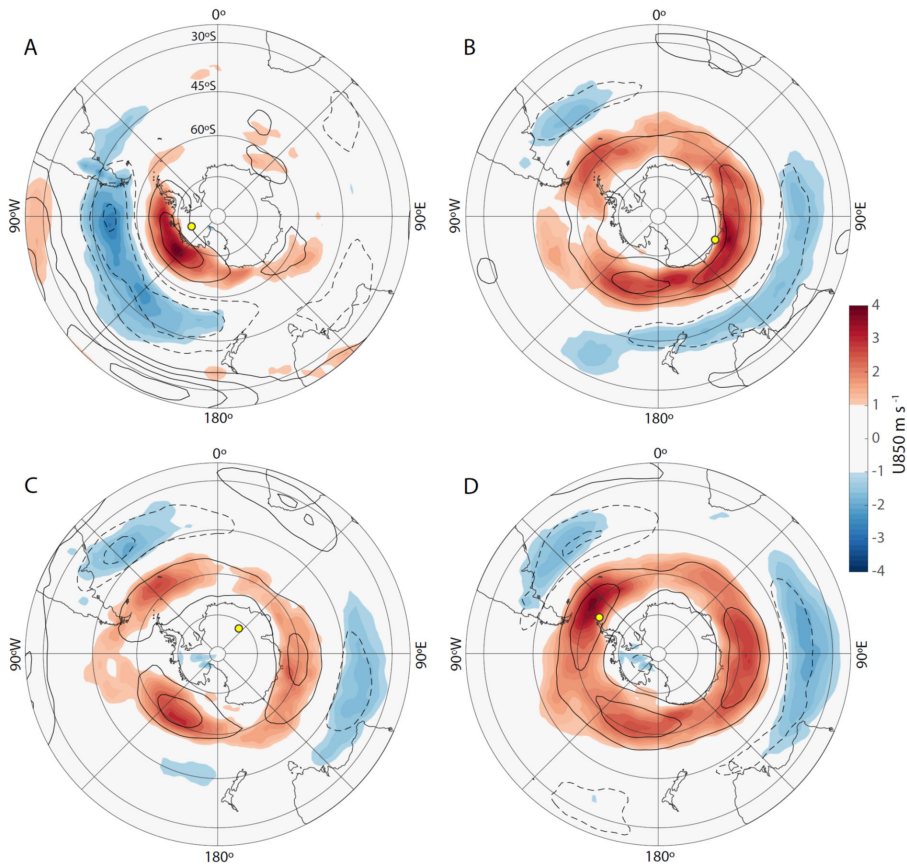
1257

Figure 4. Zonal wind speed at 850 hPa (color shading, see scale bar) and 200 hPa (2 m s^{-1} contours) regressed onto surface synoptic activity Φ at the Antarctic ice core sites of: **A** WAIS Divide; **B** Law Dome (DE08, DE08-OH and DSSW20K); **C** Dome Fuji; **D** James Ross Island. Yellow dots mark the ice core locations.
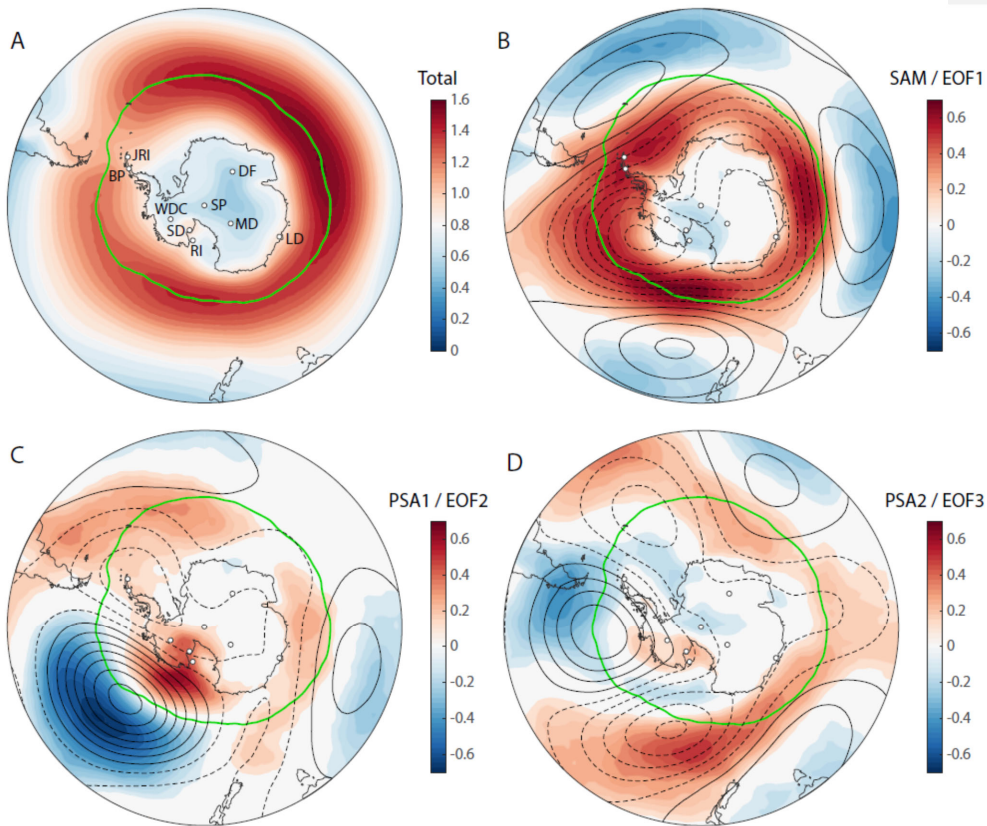
1262

Figure 5. Modes of SH extratropical atmospheric variability and their link to synoptic-scale surface pressure variability in Antarctica. **A** Annual mean Φ in units of % day^{-1}. **B** Colors show correlation between Φ and the Southern Annular Mode (SAM) index, with superimposed the 500 hPa geopotential height anomalies in 10 m contours (positive contours solid, negative contours dashed). **C** as panel B, but for the Pacific-South American Pattern 1 (PSA1). **D** As panel B, but for the Pacific-South American Pattern 2 (PSA2). SAM, PSA1 and PSA2 are defined as respectively the first, second and third EOFs (Empirical Orthogonal Functions) of the 500 hPa geopotential height anomalies in 20°-90°S monthly values in the 1979-2017 ERA interim reanalysis (Dee et al., 2011). In all panels the latitude of maximum Φ is denoted by the green line.
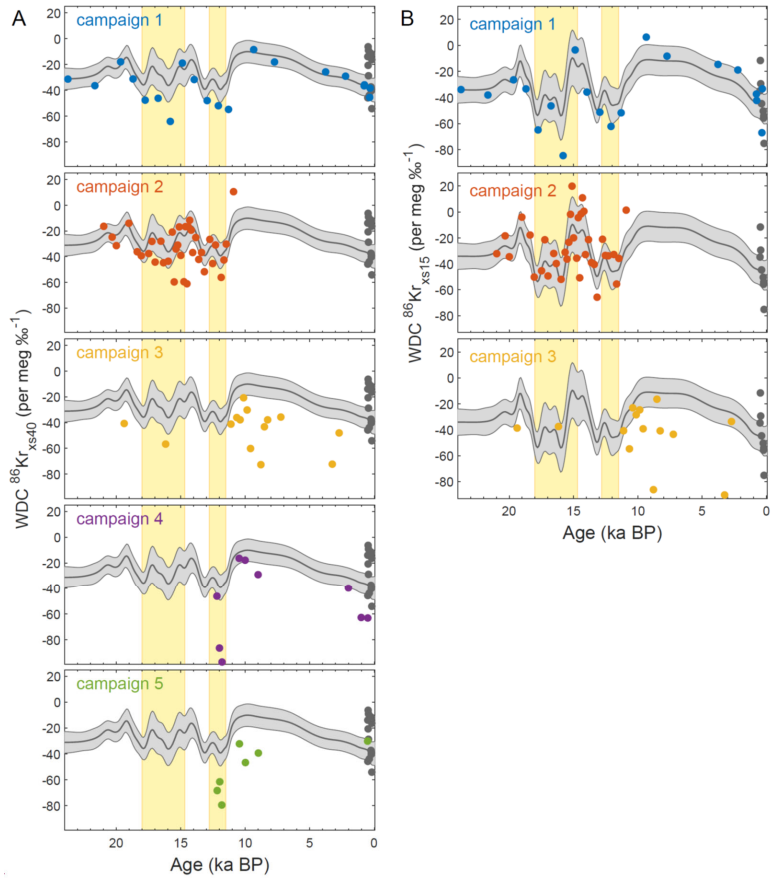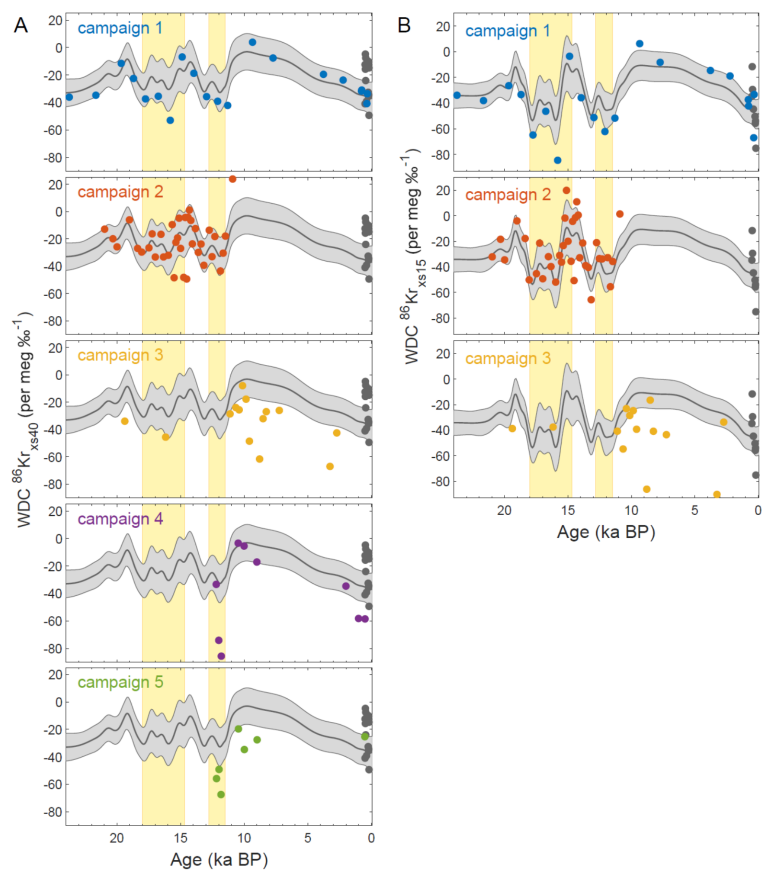
Figure 6. WAIS Divide Kr-86 excess records through the last deglaciation. **A** WDC $^{86}Kr_{xs40}$ data from the five measurement campaigns. The gray curve shows a Gaussian smoothing curve to the combined data from the first two campaigns; the light gray shaded area shows the $\pm 1\sigma$ uncertainty envelope based on a 10,000 iteration Monte-Carlo sampling of the errors and uncertainties. The WDC calibration data is shown as gray circles for comparison. **B** As in panel (A), but for $^{86}Kr_{xs15}$. For campaigns 4 and 5 the sample was not split, and no $\delta^{15}N$ data are available. The Heinrich Stadial 1 and Younger Dryas North-Atlantic cold periods marked in yellow. Thermal corrections in the WDC $^{86}Kr_{xs}$ records are based on firn model simulations.; gas-loss correction is based on a 3rd order polynomial fit to the WDC gravity-corrected $\delta O_2/N_2$ - $\delta Ar/N_2$ (Fig. A5).

1285

1286
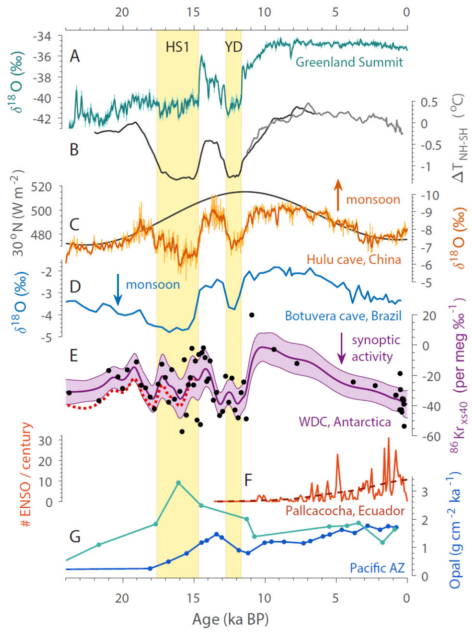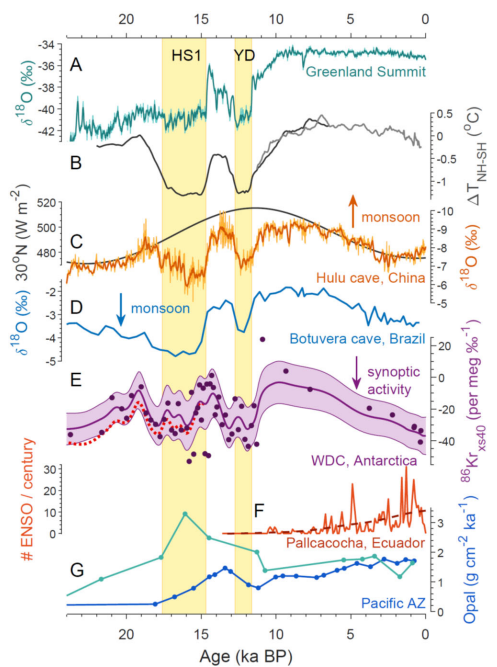
1287

Figure 7. Climate records through the last deglaciation with the Heinrich Stadial 1 (HS1) and Younger Dryas (YD) North-Atlantic cold periods marked in yellow. **A** Greenland Summit ice core stable water isotope ratio $\delta^{18}O$ here the average of the GISP2 and GRIP ice cores (Grootes et al., 1993). **B** Hemispheric temperature difference (McGee et al., 2014) based on global proxy compilations for the Holocene (Marcott et al., 2013) and last deglaciation (Shakun et al., 2012). **C** Speleothem calcite $\delta^{18}O$ from Hulu and Dongge Caves, China, as a proxy for East Asian summer monsoon strength (Dykoski et al., 2005; Wang et al., 2001). Superimposed is summer solstice (June 21) insolation at 30ºN. **D** Speleothem calcite $\delta^{18}O$ from Botuvera cave, southern Brazil, as a proxy for South American summer monsoon strength (Cruz et al., 2005; Wang et al., 2007). **E** Kr-86 excess record from WAIS Divide (this study); corrected for gas loss and thermal fractionation (Appendix A). Center line and shaded envelope show the mean and $\pm1\sigma$ uncertainty interval of a 10,000 iteration Monte Carlo smoothing exercise (see text). The dotted red line equals the center line with a correction for elevation change applied (Appendix A) using a simulated elevation history (Golledge et al., 2014). **F** Number of El Niño events per century from laminations in sediments from Laguna Pallcacocha, Ecuador (Moy et al., 2002). **G** Th-normalized opal flux in the Pacific Antarctic zone (south of the polar front) from cores NBP9802-6PC1 (turquoise; 169.98ºW, 61.88ºS) and PS75/072-4 (blue; 151.22ºW, 57.56ºS), reflecting local productivity and (wind-driven) upwelling (Chase et al., 2003; Studer et al., 2015). All isotope data in this figure are on the V-SMOW scale. Arrows show direction of increased monsoon strength / synoptic activity.
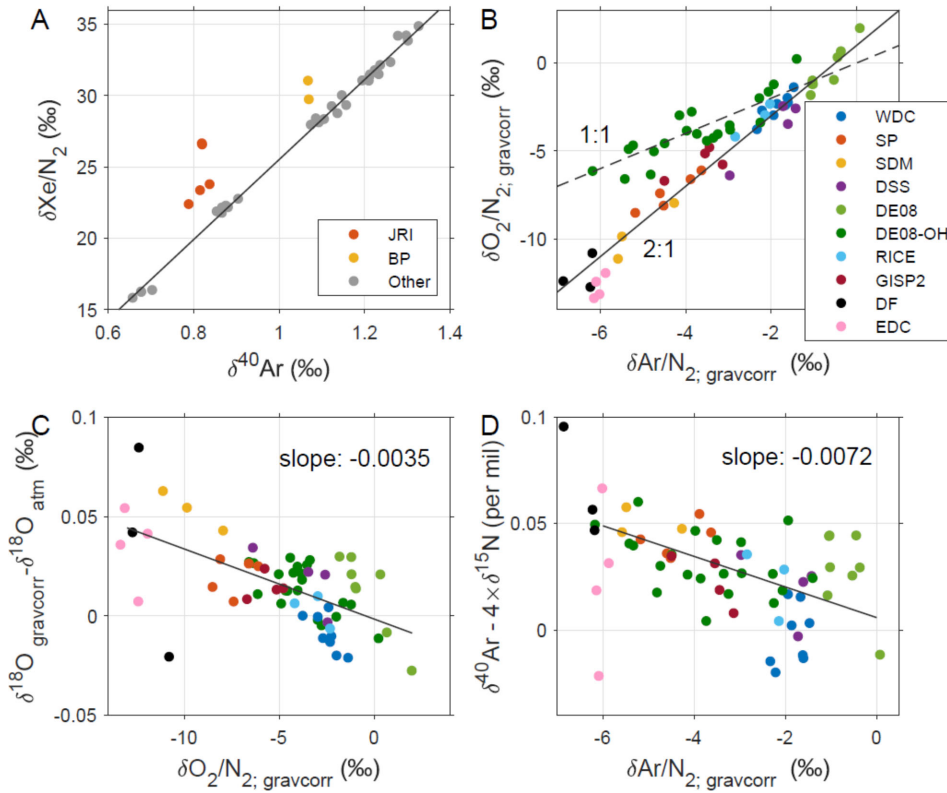
Figure A1. Elemental ratios in the 11-site calibration study of late Holocene samples. **A** $\delta Xe/N_2$ vs. $\delta^{40}Ar$
in all ice core samples. $\delta^{40}Ar$ is used solely to illustrate gravitational enrichment, and a similar picture arises
when plotted against any isotopic pair. Refrozen meltwater (elevated $\delta Xe/N_2$) was seen in all samples from
the Antarctic Peninsula (James Ross Island and Bruce Plateau sites), despite selecting samples free of
visible melt features. **B** The relationship between the commonly used gas loss proxies $\delta O_2/N_2$ and $\delta Ar/N_2$
corrected for gravity. **C** Enrichment in $\delta^{18}O$ (corrected for gravity and atmospheric $\delta^{18}O_{atm}$) plotted against
gravity-corrected $\delta O_2/N_2$ **D** $\delta^{40}Ar$ enrichment plotted against gravity-corrected $\delta Ar/N_2$. In all panels
gravitational correction is applied by subtracting $\delta^{15}N$ times the atomic mass unit difference.
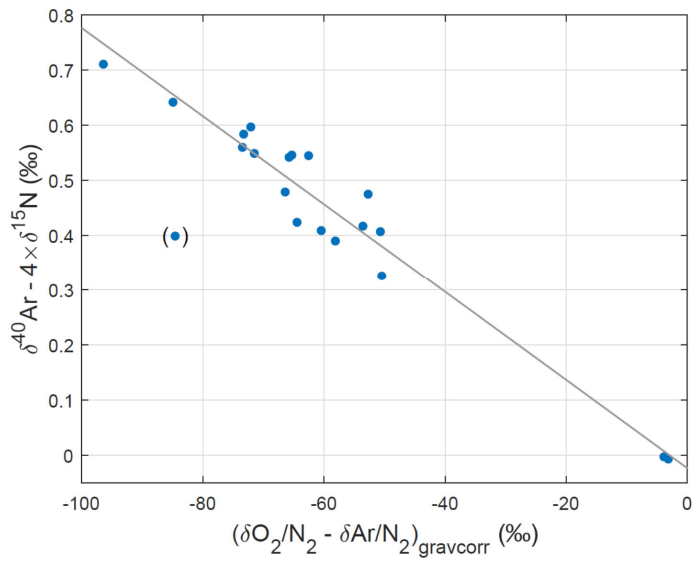
1315

Figure A2. Argon isotopic enrichment due to gas loss in the Byrd core used to determine the δ^{40}Ar gas loss correction (appendix A1). The enrichment in δ^{40}Ar plotted as a function of gravitationally corrected ($\delta O_2/N_2$ - $\delta Ar/N_2$) measured in the deep Antarctic Byrd ice core, which suffered heavy gas loss. Ice samples were analyzed in the Bender Lab at the University of Rhode Island by Jeff Severinghaus in 1997. The slope of the least-square fit is ε_{40} = -0.008. The data point in parentheses is treated as an outlier and excluded from the fitting.

1322
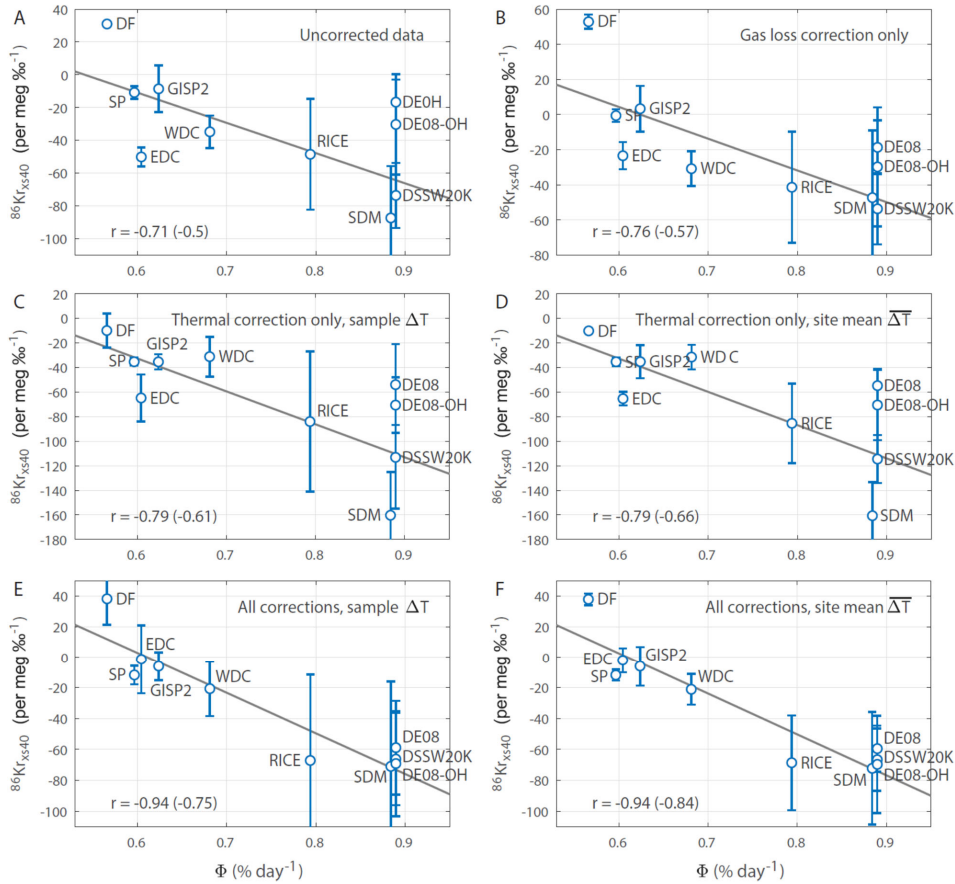
1323

1324

Figure A3. Influence of gas loss and thermal correction on the $^{86}Kr_{xs40}$ calibration. We plot $^{86}Kr_{xs40}$ as a function of Φ **A** without any data corrections applied; **B** with only the gas loss correction applied (ε_{40} = -0.008); **C** with only the thermal correction applied using individual sample ΔT; **D** with only the thermal correction applied using individual site mean $\overline{\Delta T}$; **E** with both gas loss and thermal corrections applied using individual sample ΔT; **F** with both gas loss and thermal corrections applied using site mean $\overline{\Delta T}$. In each panel the correlation to Φ are listed for the site-average and individual sample with the latter in parentheses. For all correlations $p < 0.05$.
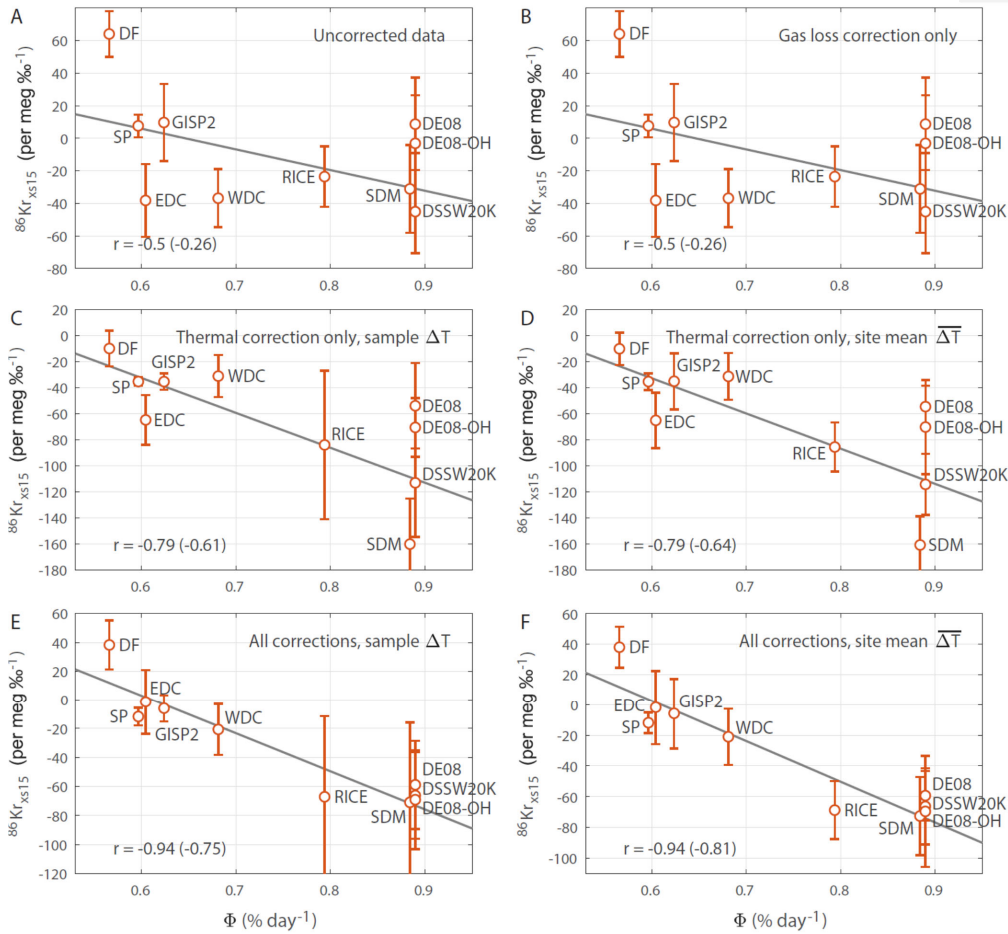
1332

Figure A4. Same as figure A3, but for $^{86}Kr_{xs15}$. Note that the gas loss correction (panel B) does not impact $^{86}Kr_{xs15}$. For all correlations $p < 0.05$, except for panels **A** and **B** where $p = 0.16$ for the site-average correlation.

 Figure —— A5.

1338
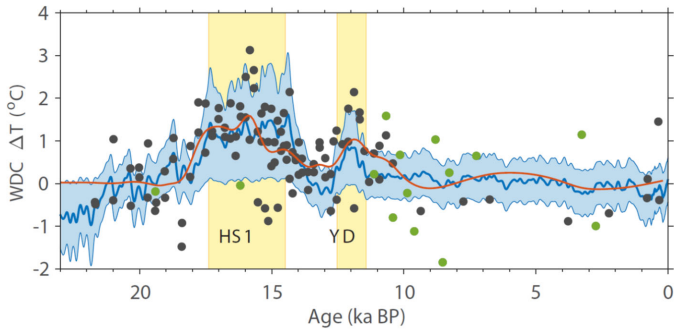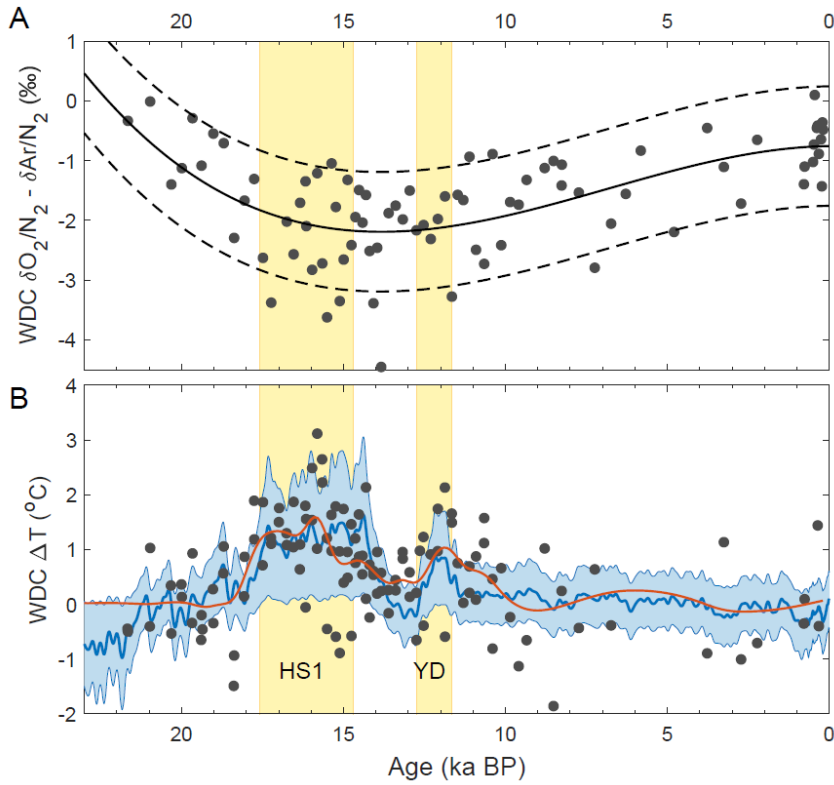
1339 **Figure A5.** Gas loss and thermal corrections for the WDC time series. **A.** WDC gravity-corrected $\delta O_2/N_2$
1340 - $\delta Ar/N_2$, as a measure of gas loss. The solid line is a third-order polynomial fit to the data; the dashed lines

1341 give a ± 1‰ range around the fit, which captures the majority of the data. **B.** The ΔT correction applied to
1342 the downcore records. Blue envelope shows the $\pm 2\sigma$ range of thermal correction scenarios in the Monte
1343 Carlo sampling, together with the mean (blue line). Gray dots show WDC ΔT estimates from available [15]N-
1344 excess data, with the red curve being a Gaussian smoothing function to the data. ~~Green dots are~~ [15]~~N-excess~~
1345 ~~from campaign 3, showing somewhat greater scatter,~~

1346
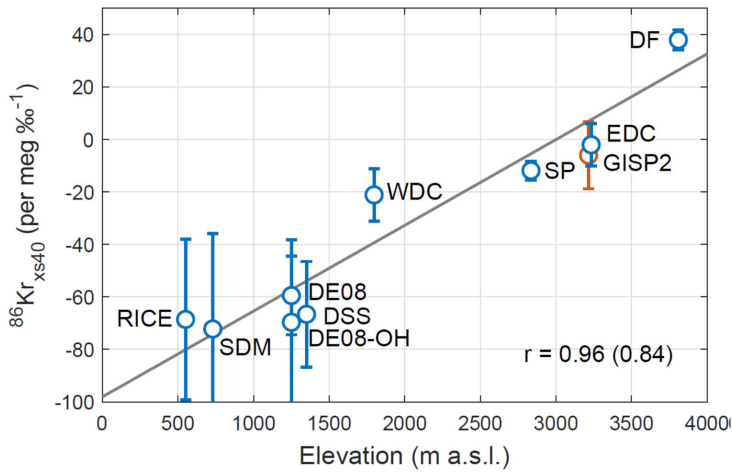
1347

1348 **Figure A6.** Kr-86 excess dependence on site elevation. Vertical axis is the [86]Kr_{xs}. The linear fit has a slope
1349 of 34 per meg ‰$^{-1}$ per 1000 m elevation.
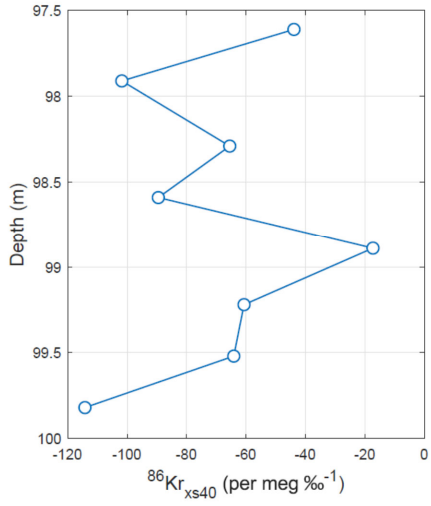
1350

1351 **Figure B1** High-resolution sub-annual sampling of $^{86}Kr_{xs40}$ in the DE08-OH site. The annual layer thickness
1352 at this depth is around 1.3 m.

1353 **Table 1.** Ice core sites used in this study, with N the number of samples included in the calibration study.
1354 See the main text for acronyms.
1355

Site	T (°C)	A (m ice a^{-1})	Φ (% day^{-1})	Latitude	Longitude	N
WDC	-31	0.22	0.68	79.5°S	112.1°W	8[a]
DF	-57	0.028	0.56	77.3°S	39.7°E	3
SP	-51	0.078	0.6	90.0°S	98.2°W	5
SDM	-25	0.13	0.88	81.7°S	149.1°W	3
DSSW20K	-21	0.16	0.89	66.8°S	112.6°E	4
DE08	-19	1.2	0.89	66.7°S	113.2°E	8
DE08-OH	-19	1.2	0.89	66.7°S	113.2°E	8[b]
RICE	-24	0.24	0.79	79.4°S	161.7°W	3[a]
EDC	-55	0.03	0.6	75.1°S	123.4°E	4
JRI	-14	0.68	0.97	64.2°S	57.7°W	5[c]
BRP	-15	2	0.9	66.1°S	64.1°W	2[c]
GISP2	-32	0.23	0.62	72.6°N	38.5°W	4

1356 [a] Not including one sample rejected due to technical problems.
1357 [b] Only shallow samples due to strong gas loss in deeper samples attributed to warm storage conditions.
1358 [c] Refrozen meltwater present as indicated by elevated Xe/N_2 ratio.
1359
1360
1361
1362
1363 **Table 2.** Pearson correlation between Φ at the ice coring sites and large-scale atmospheric circulation.
1364 Correlations are calculated using annual mean data (all months, April-March). We only list the
1365 statistically significant correlations ($p < 0.1$). The Niño 3.4 is calculated over 5°S - 5°N, 190°E - 240°E,
1366 using SST from Huang et al. (2014); the PDO index is from Mantua and Hare (2002).
1367

Site	SAM	PSA1	PSA2	Niño 3.4	PDO	Sea ice Am-Bell	Sea ice Ross
WDC	-	0.31	-	0.31	0.28	-	-
SDM	-	0.47	0.34	0.43	0.45	-	-0.32
RICE	-	0.41	0.34	0.34	0.45	-	-0.30
SP	-	-	-0.32	-	-0.30	-	-
LD	0.45	-	-	-	-	-	-
DF	0.37	-	-	-	-	-	-
EDC	0.30	-	-	-	-	-	-
JRI	0.67	-	-	-	-	0.31	-
BRP	0.68	-	-	-	-	-	-

1368
1369
1370